Study of the performance of SiO$_2$-supported Mo$_2$C and metal-promoted Mo$_2$C catalysts for the hydrodeoxygenation of *m*-cresol

Leticia F. Sosa [a,b], Priscilla M. de Souza [b], Raphaela A. Rafael [b], Robert Wojcieszak [b], Valérie Briois [c], Lucas R. Francisco [d,e], Raimundo C. Rabelo-Neto [d], Eric Marceau [b], Sébastien Paul [b], Fabio S. Toniolo [a], Fabio B. Noronha [b,d,e,*]

[a] *Federal University of Rio de Janeiro, Chemical Engineering Program of COPPE/UFRJ, P.O. Box 68502, CEP 21941-972, Rio de Janeiro, Brazil*
[b] *Univ. Lille, CNRS, Centrale Lille, Univ. Artois, UMR 8181 - UCCS - Unité de Catalyse et Chimie du Solide, F-59000 Lille, France*
[c] *Synchrotron SOLEIL, L'Orme des Merisiers, Saint-Aubin, BP 48, 91192 Gif-sur-Yvette Cedex, France*
[d] *National Institute of Technology, Catalysis, Biocatalysis and Chemical Processes Division, Av. Venezuela 82, 20081-312, Rio de Janeiro, RJ, Brazil*
[e] *Military Institute of Engineering, Chemical Engineering Department, Praça Gal. Tiburcio 80, Rio de Janeiro, 22290–270, Brazil*

A R T I C L E I N F O

A B S T R A C T

The performance of Mo$_2$C, Mo$_2$C/SiO$_2$, Ni-Mo$_x$C$_y$/SiO$_2$, and Cu-Mo$_x$C$_y$/SiO$_2$ catalysts for the hydrodeoxygenation of *m*-cresol at 300 °C and atmospheric pressure was investigated. Ni/SiO$_2$ and Cu/SiO$_2$ were used as references. To get more insight into the effect of the promoters during the synthesis of the Mo carbides, the carburization of the supported catalysts was followed by X-ray spectroscopy under 20 % (v/v) CH$_4$/H$_2$. The results showed that the presence of a second metal promotes the first step of reduction, and it is related to the crystallinity of the mixed molybdates in the initial promoter species, but that it does not assist the carburizing step. All carbides were highly selective to toluene (> 96 %), indicating that Mo$_2$C species is the active site responsible for the deoxygenation of *m*-cresol. Mo$_2$C/SiO$_2$ catalyst carburized at 400 °C was inactive, which is due to the lower oxophilicity of the oxycarbide species (MoO$_{2-x}$C$_x$).

1. Introduction

In the last decades, lignocellulosic biomass has been pointed out as a potential sustainable raw material for the production of energy, biofuels, and chemicals of industrial interest [1]. The fast pyrolysis of lignocellulosic biomass generates bio-oil, which can be used for the production of hydrocarbons that are compatible with petroleum-derived fuels. However, large amounts of oxygen-rich phenolic compounds such as cresol, guaiacol, and phenol can be found in bio-oils. The high content of oxygen gives undesirable properties to bio-oil, like a low calorific value, high acidity, and viscosity, and thermal and chemical instability. Catalytic hydrodeoxygenation (HDO) is thus a key step to upgrading bio-oil to liquid fuels by decreasing its oxygen content [2,3].

Since lignin-derived bio-oil mainly contains functionalized aromatic compounds, the design of new catalysts for the HDO reaction is often based on model reactions involving aromatic molecules that bear hydroxyl and methoxy functional groups, such as phenol [4], cresol [5], anisole [6] and guaiacol [7]. According to these studies, a bifunctional catalyst containing (i) metal particles to carry out hydrogenation/hydrogenolysis reactions and (ii) a support assisting deoxygenation is required for the HDO of phenolic compounds [2].

Recently, transition metal carbides have aroused great interest for their high selectivity to arenes in HDO of phenolics compounds [2, 8–10]. For this reason, they have been investigated for HDO reactions of bio-oil [11–14] and several phenolic compounds such as phenol [15–17], cresols [18,19], anisole [20–24], and guaiacol [25–30].

On the other hand, the use of bimetallic carbides for the HDO of phenolic molecules has been reported to be beneficial but remains scarce [23,31–33]. A study combining experimental measurements and Density Functional Theory (DFT) calculations was used to investigate the HDO of guaiacol over Mo$_2$C and MoWC catalysts. The bimetallic Mo-W catalyst exhibited a higher selectivity to deoxygenated products (benzene and toluene) [31,33]. DFT calculations demonstrated that oxygen is more strongly adsorbed on MoW than on non-promoted carbide,

---

confirming the higher oxophilicity of the bimetallic carbide. In another study, Ni-Mo$_2$C/SBA-15 exhibited a high activity for HDO of *m*-cresol in liquid phase, with the formation of methylcyclohexane and methyl-cyclohexanol [32]. However, its performance was not compared with that of Ni/SBA-15 or Mo$_2$C/SBA-15 monometallic catalysts. Therefore, the effect of Ni on the nature of the carbide phase and on the mechanism of HDO reaction of *m*-cresol was not explained. Ni$_x$MoC/SiO$_2$ catalysts with different Ni content were tested for HDO of anisole in liquid phase [23]. XRD showed the presence of three different phases: β-Mo$_2$C; Mo$_3$Ni$_2$C and NiMo alloy with different compositions. Increasing the NiMo alloy content increased the activity for hydrogenation. However, the extent of HDO reaction achieved a maximum for Ni$_x$MoC/SiO$_2$ catalysts with low Ni content (x = 0.5 and 1.0). Although only Ni and W have been used as promoters of Mo carbide catalysts in the HDO reaction of phenolic molecules, the addition of other metals has improved the performance of Mo$_2$C in other reactions. For instance, Cu has been reported to improve the activity of the Mo carbide for CO$_2$ hydrogenation reaction by providing a higher molecular hydrogen availability [34–36]. The effect of Cu addition on the performance of molybdenum carbide catalysts for the HDO of *m*-cresol has not been reported in the literature.

The high selectivity to deoxygenated products of the carbide phase has been attributed to its high oxophilicity, required for the adsorption of the oxygen atom from the oxygenated molecule. However, the active phase responsible for the high deoxygenation activity of non-promoted Mo carbide catalysts are still under debate, especially for bimetallic systems. For instance, the oxygen content of the Mo carbide phase has been thought to be a critical parameter in determining selectivities. Wang et al. [19] proposed that Mo$_2$C and MoO$_x$C$_y$ needed to co-exist for the HDO of *p*-cresol. On the opposite, Chen and Bhan [18] reported that adsorbed oxygen poisons the metal-like sites responsible for the deoxygenation of *m*-cresol. For the HDO of anisole [21] and guaiacol [31] over Mo$_2$C, the presence of two sites has been proposed: one responsible for hydrogen activation and an oxophilic site where the activation of the oxygenated compound occurs. In the case of promoted metal carbides, the identification of active phases is more complex with several open questions. Does the formation of a bimetallic carbide occur or are isolated metallic particles in contact with the metal carbide formed? Therefore, *in situ* characterization of Mo$_2$C-based catalysts is fundamental to determining a structure-performance relationship.

Traditionally, transition metal carbides are prepared by temperature-programmed carburization (TPC), in which a metal oxide is heated at a specific rate in a carburizing atmosphere of CO or a hydrocarbon (CH$_4$, C$_2$H$_6$, C$_3$H$_8$, C$_4$H$_{10}$) used as a carbon source, co-fed or not with hydrogen and the products are followed by mass spectroscopy [37].

The carburization of MoO$_3$ under 20 (v/v) % of methane in hydrogen has been proposed to occur in two steps by mass spectroscopy. The first step has been attributed to the reduction of MoO$_3$ to MoO$_2$, while the second one to the simultaneous reduction and carburization of MoO$_2$ to β-Mo$_2$C [38]. In the case of bimetallic carbide catalysts, mass spectroscopy does not allow to identify the different species formed due to the complex profiles produced during carburization that are characterized by the presence of multiples peaks. Therefore, the role of the second metal in the formation of the active phase is not yet clear. Does the second metal promote the first step of MoO$_3$ reduction as well as the carburization of Mo oxide at higher temperatures? Does the promoter interact with carbide phase? Does the nature of the second metal affect the formation of Mo carbide phase differently?

X-ray absorption spectroscopy (XAS) is a powerful technique that allows the monitoring of the species formed during the *in situ* carburization and under reaction conditions [39–41]. Zhu et al. [41] carried out *in situ* XAS experiments during the carburization of molybdenum carbide catalyst supported on activated carbon and the HDO of anisole at different temperatures to establish a correlation between the active phase and activity and products distribution. Benzene and phenol were the main products formed over oxycarbide sites (MoO$_x$C$_y$ species), whereas carbides sites (α-MoC$_{1-x}$ and β-Mo$_2$C species) promoted the

direct deoxygenation of anisole to benzene. To the best of our knowledge, save for this study, XAS analysis has been used to characterize promoted monometallic molybdenum carbide catalysts only after their synthesis [42,43], but not during carburization, and no study has been reported on promoted Mo carbides, and on the role and chemical state of the promoter.

Therefore, our work aimed to study the carburization of SiO$_2$-supported molybdenum carbides using *in situ* XAS experiments and Multivariate Curve Resolution by Alternative-Least Squares (MCR-ALS) methodology to shed light on the species formed during carburization on non-promoted and promoted (Ni, Cu) systems. In the immediate aftermath of carburization, the molybdenum carbide catalysts were tested for the HDO of *m*-cresol reaction in the gas phase. This approach allowed us to establish a structure-performance relationship for these catalysts.

2. Experimental

2.1. Catalyst preparation

In this work, silica (SiO$_2$, Aerosil 200, Evonik Industries) was used as support. The material was moistened with deionized water, dried under static air for 3 h at 120 ºC, and heated at 500 ºC (10 ºC min^{-1}) for 6 h. The precursors of the monometallic and Ni/Cu promoted molybdenum carbides supported on silica (Mo$_2$C/SiO$_2$, Ni-Mo$_x$C$_y$/SiO$_2$, and Cu-Mo$_x$C$_y$/SiO$_2$) were prepared by incipient wetness impregnation of the support to achieve 20 wt. % of active phase (20 wt. % for the monometallic and 17 wt. % Mo and 3 wt. % Ni or Cu for the promoted materials).

To prepare the monometallic carbide, an adequate amount of ammonium heptamolybdate ((NH$_4$)$_6$Mo$_7$O$_{24}$.4H$_2$O, Sigma-Aldrich) was first solubilized in distilled water and then the solution obtained (0.173 g mL^{-1}) was impregnated onto the support. After impregnation, a final drying was performed at 110 °C overnight.

For the promoted catalysts, adequate amounts of nickel nitrate (Ni (NO$_3$)$_2$.6H$_2$O, Sigma-Aldrich) or copper nitrate (Cu(NO$_3$)$_2$·H$_2$O, Sigma-Aldrich) and ammonium heptamolybdate ((NH$_4$)$_6$Mo$_7$O$_{24}$.4H$_2$O, Sigma-Aldrich) were solubilized individually in distilled water at the concentrations of 0.076, 0.045 and 0.16 g mL^{-1}, respectively. Firstly, the solution containing Mo was impregnated on the support, the solid was dried overnight at 110 °C and then the solution containing Ni or Cu was added using the same procedure.

For the sake of comparison, two reference catalysts containing 3 wt. % of Ni or Cu supported on SiO$_2$ were prepared by incipient wetness impregnation. For this, adequate amounts of nickel nitrate (Ni(NO$_3$)$_2$.6 H$_2$O, Sigma-Aldrich) or copper nitrate (Cu(NO$_3$)$_2$·H$_2$O, Sigma-Aldrich) were solubilized in distilled water at the concentrations of 0.117 and 0.087 g mL^{-1}, respectively, and then each solution was impregnated individually on the support. After impregnation, the materials were dried at 110 °C overnight. Finally, all samples were treated under static air at 500 °C (5 °C min^{-1}) for 3 h to obtain the calcined precursors.

To synthesize an unsupported Mo carbide, or the SiO$_2$-supported Mo carbides, the molybdenum trioxide (MoO$_3$, Sigma-Aldrich) or calcined precursors, respectively, were carburized at 650 °C (2.5 °C min^{-1}) for 2 h using a ratio of 2:1 of mass of catalyst and flow rate of CH$_4$/H$_2$ mixture (20 % (v/v)) [44]. The carbides were designated as Mo$_2$C, Mo$_2$C/SiO$_2$, Ni-Mo$_x$C$_y$/SiO$_2$, and Cu-Mo$_x$C$_y$/SiO$_2$. The reference catalysts (MoO$_3$, Ni/SiO$_2$ and Cu/SiO$_2$) were reduced under pure hydrogen at 650 °C (2.5 °C min^{-1}) for 2 h. The catalysts were passivated at room temperature for 14 h with 0.5 % (v/v) O$_2$/N$_2$ (30 mL min^{-1} STP) due to their pyrophoric nature before being characterized by inductively coupled plasma optical emission spectrometry, elemental analysis, and N$_2$ physisorption.

2.2. Catalyst characterization

The amounts of Mo, Ni, and Cu in the carbides were determined by inductively coupled plasma optical emission spectrometry (ICP-OES)

using a 720-ES ICP-OES spectrometer (Agilent) with axial viewing and simultaneous CCD detection. The content of carbon was determined by elemental analysis using a Thermo Scientific FlashSmart automated analyzer.

Textural properties of SiO_2 and passivated catalysts were measured by nitrogen adsorption at $-196\ °C$ using a Micromeritics TriStar II Plus analyzer. The samples were previously outgassed under vacuum firstly at 75 °C for 1 h and then at 300 °C for up to 24 h. Specific surface areas and the total pore volume were estimated using the Brunauer-Emmett-Teller (BET) and the Barrett-Joyner-Halenda (BJH) methods, respectively.

X-ray absorption spectroscopy (XAS) was carried out in the transmission mode at the ROCK Quick-EXAFS beamline at the French synchrotron radiation facility SOLEIL [45]. The beamline benefits from a 2.81 Tesla Super-Bend source which delivers nearly 10^{12} ph s^{-1} between 8 and 20 keV. Spectra were acquired under *in situ* conditions, either at the Mo K-edge for monometallic systems, or alternatively at the Ni (8333 eV), Cu (8979 eV), and Mo K-edges (20,000 eV) for the bimetallic Ni-Mo and Cu-Mo systems during carburization under 20 % (v/v) CH_4/H_2. The monochromator used is based on a Si (111) channel-cut installed on a tilt table allowed to oscillate around the Bragg angle characteristic of the element of interest, *i.e.*, 13.4332° for Ni, 12.2886° for Cu, and 5.6550° for Mo, with an amplitude of 2.0° for Ni and Cu and 0.5° for Mo. The Si (111) channel-cut oscillation frequency was set to 2 Hz and recorded two quick-EXAFS spectra every 0.5 s. Every 10 acquired spectra were merged to improve the signal/noise ratio. Ionization chambers were filled with nitrogen for Ni and Cu K edges measurements and a mixture of 50:50 of nitrogen and argon for the Mo K edge measurements. The beam size at the sample position was ~ 500 μm (H) x 300 μm (V).

Experiments were performed using a dedicated gas-feeding set-up installed on the ROCK beamline [46]. A quartz capillary (1.5 mm × 80 mm x 0.04 mm) was used as a sample holder. The powder catalyst bed (length ~ 8–9 mm) was maintained at the center of the capillary between two pieces of quartz wool and heated using a gas blower. Raman spectra were measured at room temperature on the catalyst bed using a commercial RXN1 Raman spectrometer (Kaiser Optical Systems, Inc.). The *in situ* temperature programmed carburization of the calcined precursors was performed by heating the capillary from room temperature to 650 °C (2.5 °C min^{-1}) under a 20 % (v/v) CH_4/H_2 flow (5 mL min^{-1} STP). Spectra were then recorded back at room temperature. A passivated β-Mo_2C used as reference was reactivated at 400 °C (5 °C min^{-1}) under pure H_2 (5 mL min^{-1} STP).

Energy calibration concerning the reference metal foil (Mo, Ni, Cu) and a XAS data-normalization procedure was first carried out using the Python normal graphical interface developed at SOLEIL for the fast handling of Quick-XAS data [47]. The EXAFS signal extraction and Fourier transform of the EXAFS spectra was done using the Athena graphical interface software [48]. EXAFS fitting of coordination numbers (N), Debye-Waller factors (σ^2), and interatomic distances (R) were simultaneously performed on k-, k^2-, and k^3-weighted χ(k) functions with the Artemis interface to IFeFFIT using least-squares refinements [49]. Fits were first performed on the metallic foil references for the determination of the S$_0^2$ factor. Fourier-transformed EXAFS signals are presented as k^3-χ(k) functions and Fourier transforms are shown without phase correction.

The proportions of different Mo, Ni, and Cu species during the different stages of carburization were determined by a chemometric procedure, the Multivariate Curve Resolution by Alternative-Least Squares (MCR-ALS) methodology, using the free MCR-ALS GUI 2.0 toolbox developed by the Tauler group on the Matlab platform [50]. XAS spectra are considered to be linear combinations of individual spectral components (matrix S) weighted by their concentration that varies with temperature or time (matrix C). The determination of matrices S and C takes place without initial hypotheses on the chemical nature of the different species appearing along the thermal treatment, by a

least-square minimization of a residue matrix. The determination of the most likely number of spectral components takes place *via* a preliminary Principal Component Analysis by Singular-Value Decomposition (PCA-SVD). MCR-ALS spectral components (XANES spectra, EXAFS oscillations, and Fourier transform) are then identified to successive species after checking their chemical meaningfulness, by comparison with spectra of compounds already known in the mixture or as standards, or with plausible models in accordance with the chemistry of the system. Further details about the MCR-ALS method applied to XAS are available in recent publications [47,51,52].

The synthesis of carbides was also followed by temperature-programmed carburization (TPC) in another experiment carried out in a multipurpose unit equipped with an oven operated by a temperature controller (Therma, model TH2031P) and coupled to a Pfeiffer Vacuum mass spectrometer (MS) model QME 200. Before analysis, the calcined precursors (0.1 g) were placed in a quartz reactor fitted in the unit and treated under He (50 mL min^{-1} STP) at 200 °C (10 °C min^{-1}) for 1 h to eliminate water and then cooled down to 30 °C. Then, He was replaced by 20 % (v/v) CH_4/H_2 (100 mL min^{-1} STP) and then, the temperature was increased up to 800 °C (2.5 °C min^{-1}). The signals of the ions $m/z = 18$ (H_2O), $m/z = 15$ (CH_4) and $m/z = 28$ (CO) were continuously monitored on the mass spectrometer, in which a small aliquot is admitted *via* a leak valve (Granville-Phillips).

2.3. Catalytic evaluation

The HDO of the *m*-cresol reaction was performed in a vapor-phase fixed-bed flow reactor system, operating at atmospheric pressure of H_2 and 300 °C. The samples were mixed with silicon carbide ($m_{SiC}/m_{catalyst} = 3.0$) to make the flow more uniform and to avoid hot spot formation or flow channeling. The catalysts were synthesized under the conditions described in Section 2.1. Then, the temperature was decreased to 300 °C and the reactant mixture was obtained by flowing 60 mL min^{-1} STP of H_2 through a saturator containing the probe molecule that was maintained at the temperature needed to produce the desired H_2/organic molecule mole ratio of 60 (87 °C).

Different W/F ratios (catalyst mass/mass flow rate of the oxygenated compound) were used for each catalyst to achieve iso-conversion. The first injection was carried out after 5 min of time-on-stream (TOS), where minimal deactivation of the catalyst was expected. The reaction products were analyzed using an Agilent Technologies GCMS (7890 A/ 5975 C), equipped with an HP-Innowax capillary column and a flame-ionization detector (FID).

The conversion, product selectivity, and HDO reaction rate were determined by the following Eqs. (1–3):

$$Conversion(\%) = \frac{mol_{feed}^0 - mol_{feed}}{mol_{feed}^0} x100 \tag{1}$$

$$Selectivity(\%) = \frac{mol_i}{mol_{feed}^0 - mol_{feed}} x100 \tag{2}$$

$$Rate_{HDO}\left(mmolg_{cat}^{-1}min^{-1}\right) = \frac{yield\,of\,deoxygenated\,product\,x\,F}{W} \tag{3}$$

where mol_{feed}^0 and mol_{feed} are the numbers of initial and after reaction moles of the organic feed respectively, mol_i is the number of moles of a given *i* product, W is the catalyst mass (g), and F is the flow rate of *m*-cresol (mmol min^{-1}).

3. Results and discussion

3.1. Characterization

The contents of Mo, Cu, Ni, and C species in the passivated catalysts estimated by ICP-OES and elemental analysis are reported in Table 1.

Table 1

Chemical composition, textural properties of the support, and passivated catalysts.

Material	Content (wt. %)					SSA[a] (m²/g)[a]	P_v[b] (cm³/g)
	Mo	C	Ni	Cu	active phase		
SiO₂	-	-	-	-	-	198	1.13
β-Mo₂C	-	-	-	-	-	13	0.00
β-Mo₂C/SiO₂	17.6	0.8	-	-	18.4	140	0.53
Ni-Mo$_x$C$_y$/SiO₂	16.0	0.9	2.8	-	19.7	142	0.60
Cu-Mo$_x$C$_y$/SiO₂	14.9	0.8	-	2.0	17.7	137	0.66
Ni/SiO₂	-	-	2.6	-	2.6	187	1.07
Cu/SiO₂	-	-	-	2.1	2.1	185	0.70

[a] Determined by the BET method.
[b] Determined by BJH method.

The C/Mo atomic ratio was found to be slightly lower than 0.5, the value expected for Mo₂C. However, measurements needed to be done on samples that were passivated to allow for their exposure to air, and do not inform on the carbon content right after carburization.

Table 1 also shows the textural properties of the support and passivated catalysts determined by N₂ physisorption. A decrease in the specific surface area (SSA) and pore volume (P_v) was observed after the synthesis of supported carbides compared to the bare support, consistent with the formation of 20 wt. % Mo₂C, which is a nonporous oxide with a very low surface area. The N₂ adsorption-desorption isotherms are displayed in Fig. S1. All supported catalysts showed a profile similar to that of bare SiO₂, which, according to IUPAC classification, corresponds to a type II isotherm, with an H1 hysteresis loop commonly obtained for materials consisting of agglomerates or compacts of approximately uniform spheres [53,54].

Since catalytic testing took place directly after carburization, conventional characterization, for instance by *ex situ* X-ray diffraction (XRD), was not possible. The formation of the supported phases was thus followed by *in situ* XAS, carried out at Mo, Ni, and Cu K-edges, with further input from Raman spectra recorded on the initial calcined samples.

The XAS data at the Mo K-edge related to the calcined precursors of Mo₂C/SiO₂, Ni-Mo$_x$C$_y$/SiO₂, and Cu-Mo$_x$C$_y$/SiO₂ are presented in Figs. S2–S4. The shape of the XANES spectra and position in energy are similar to those of the MoO₃ standard, especially for Mo₂C/SiO₂ (Fig. S2). For the two promoted catalysts, the only significant difference is the increase of intensity of the second feature after the edge, at 20,040 eV, also well visible on a spectrum reported in the literature for γ-CuMoO₄ [55].

Raman spectroscopy confirms that MoO₃ is present on the three samples, (bands at 994, 819, and 665 cm⁻¹ [56], Fig. S5), in a well-crystallized form for the precursors of Mo₂C/SiO₂ and Ni-Mo$_x$C$_y$/SiO₂, in a more poorly organized form for the precursor of Cu-Mo$_x$C$_y$/SiO₂, as evidenced by the low intensity of these bands. Raman spectroscopy also reveals the existence of a second phase on the oxide precursor of Ni-Mo$_x$C$_y$/SiO₂. The weak but well-defined band at 961 cm⁻¹ is unambiguously assigned to α-NiMoO₄ [57,58], a mixed oxide in which octahedral groups of [NiO₆] and [MoO₆] alternate. Some weak bands are also visible for the precursor of Cu-Mo$_x$C$_y$/SiO₂. The band at 960 cm⁻¹ may be attributed to CuMoO₄ [59,60], but the broad band at 930 cm⁻¹, which is expected to be thin and poorly intense for crystalline CuMoO₄ [59,60], can rather arise from molybdates with a higher degree of condensation of the molybdate units, such as in Cu₃Mo₂O₉ [61].

X-ray diffraction analysis of the calcined precursors (Fig. S6) done in ambient conditions accordingly confirms the species identified by XAS and Raman spectroscopy. MoO₃ (JCPDS 05–0508) is present in all materials, while NiMoO₄ (JCPDS 45–0142), and CuMoO₄ (JCPDS 22–0242)

and Cu₃Mo₂O₉ (JCPDS 34–0637) phases were detected for the calcined precursors of Ni-Mo$_x$C$_y$/SiO₂ and Cu-Mo$_x$C$_y$/SiO₂, respectively.

The feature at 20,040 eV (Fig. S2), the differences in the structure of the EXAFS oscillations (Fig. S3), and the differences in the shape of the peaks on the associated Fourier transforms for the promoted systems (Fig. S4) are thus linked to the presence of a mixture of MoO₃ and Ni/Cu molybdates, more crystallized in the case of Ni-Mo$_x$C$_y$/SiO₂, and less for Cu-Mo$_x$C$_y$/SiO₂. Due to the complexity of the typical oxidic environment of Mo(VI) ions (several different Mo-O distances ranging between 1.6 and 2.2 Å) and the existence of mixtures in the bimetallic systems, it was not attempted to perform EXAFS fits for the calcined precursors at the Mo K-edge.

Before analyzing the carburization process up to 650 °C, the state of Mo after carburization will be investigated here. The XAS analysis was performed on spectra recorded after cooling to room temperature (RT), still under a CH₄/H₂ atmosphere.

After carburization, the XANES spectra, EXAFS oscillations, and Fourier transforms of Mo₂C/SiO₂, Ni-Mo$_x$C$_y$/SiO₂, and Cu-Mo$_x$C$_y$/SiO₂ are very similar and resemble that of reference bulk β-Mo₂C (the unsupported sample whose structure was identified by XRD after passivation, and that was reactivated under H₂ at 400 °C before recording the XAS spectrum) (Figs. S7 – S9).

The results of the fits for the first two shells of neighbors (C and Mo atoms) are presented in Figs. 1–2 and in Table 2. They are all consistent with the formation of Mo carbides. Given the limited number of independent parameters allowed for the fit, it was chosen to fit each shell with a single contribution of C and Mo. This does not preclude the existence of several interatomic Mo-C or Mo-Mo distances in the structure of the carbide, and the distribution of Mo-C distances can explain the larger error bar for the Debye-Waller parameter obtained by fitting the C shell. It can be added that the possible presence of O atoms in the first shell was always rejected by the fits. No bulk oxycarbide phase was thus present after carburization.

The number of C atoms around Mo is found to be larger in the supported systems than in unsupported β-Mo₂C. However, it must be remembered that the number of neighboring atoms (N) and the Debye-Waller parameter (σ^2) are correlated, and here increase concomitantly. The increase of N(C) can thus be interpreted either as the sign of a C enrichment around Mo in the carbide or as an overestimation of N by the fit, compensating for a high value of σ^2. A feature that would allow favoring the hypothesis of a carbon enrichment on the supported systems is linked to the Mo-C and Mo-Mo average interatomic distances, longer by 0.012–0.020 Å than those found for the β-Mo₂C standard.

The evolution of the XAS spectra at the Mo K-edge during carburization is presented in Figs. S10–S12. The color gradient from blue to red is related to the increase in temperature, from 30° to 650°C. It is seen that molybdenum is transformed almost continuously during the temperature ramp under CH₄/H₂, till the Mo carbide is ultimately formed. Qualitatively speaking, one can observe that the first strong shift of the spectra to lower energies (first stage of Mo reduction), along with the appearance of a poorly intense white line at 20,020 eV, occurs in a lower temperature range for Cu-Mo$_x$C$_y$/SiO₂ (light blue color) than for Mo₂C/SiO₂ and Ni-Mo$_x$C$_y$/SiO₂ (green color).

An analysis of the evolution of Mo speciation was carried out using an MCR-ALS procedure. Each experimental spectrum in the series is considered to be a linear combination of a set of independent, successive spectral components, and the MCR-ALS algorithm extracts both the matrix of spectral components and a matrix of associated "concentrations" evolving with the rising temperature. The spectral components are analyzed using the XAS toolbox, to identify the chemical species (if the spectral component is characteristic of a known species), or, as will also be the case here, to obtain spectroscopic or structural footprints of the successive species involved in the carburization process (if the spectral component cannot be associated with a recognizable chemical species or corresponds to a mixture).

The MCR-ALS procedure could evidence four distinct spectral
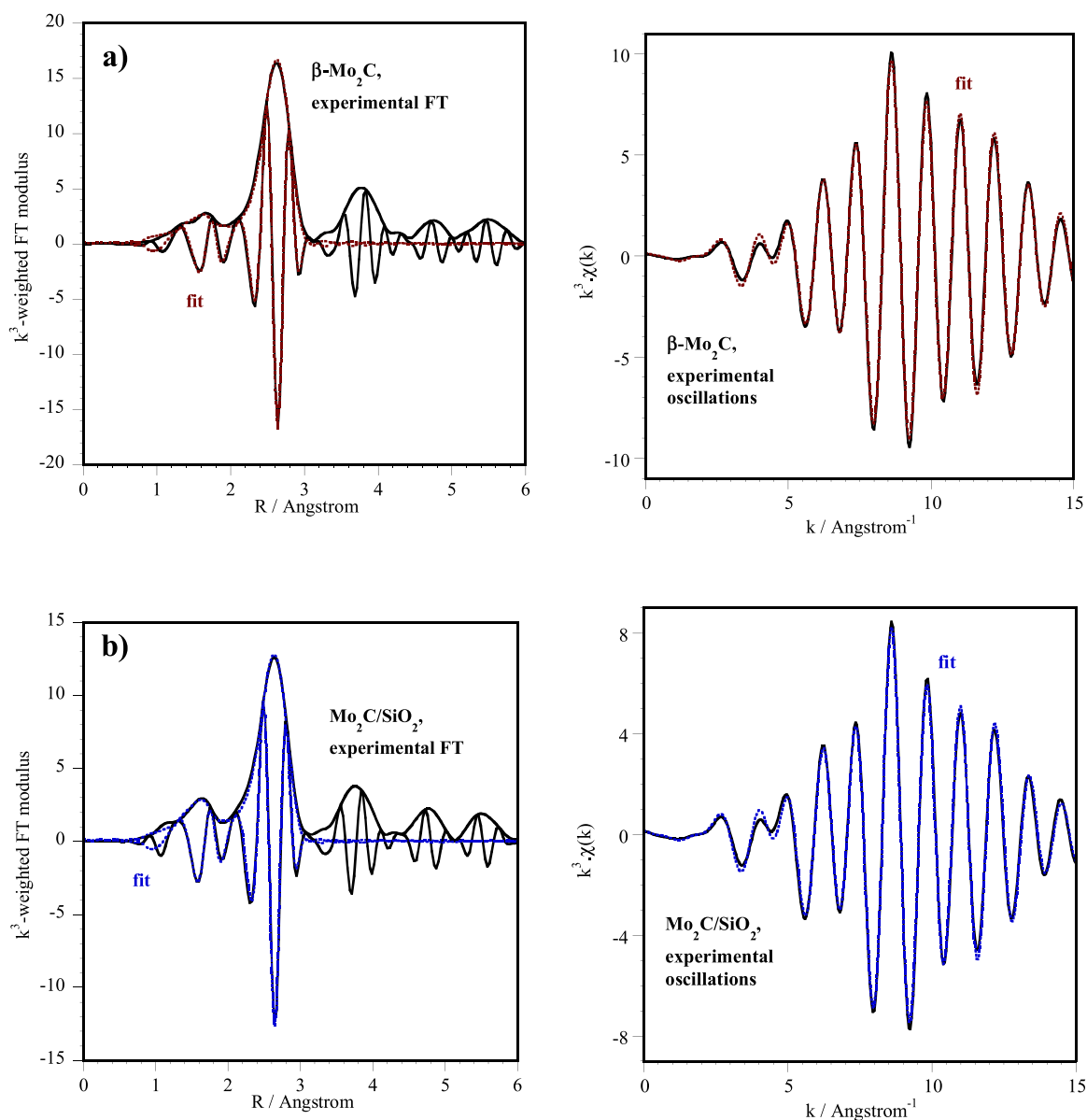
Fig. 1. XAS data at the Mo K-edge after carburization of a) β-Mo₂C after reactivation in H₂ at 400 °C, and b) Mo₂C/SiO₂ (spectra recorded at room temperature). The fit of the first and second shells of neighbors: Fourier transform (left) and EXAFS oscillations (right). k = 3.5–15 Å⁻¹.

components in each of the three carburization processes. The first of them corresponds to the spectrum of the initial, calcined precursor (Fig. S13), representing MoO_3 for Mo_2C/SiO_2, and a mixture of MoO_3 and Ni/Cu-Mo(VI) molybdates for $Ni-Mo_xC_y/SiO_2$ and $Cu-Mo_xC_y/SiO_2$. This component will be denoted as representing "Mo(VI) oxides" collectively.

For the three samples, the second spectral component (Fig. S14) is characterized by a significant shift of the edge toward lower energies compared with MoO_3, implying a decrease in the average oxidation state of Mo. This shift can be better observed when plotting the derivative of the absorbance as a function of the energy (Fig. S14b). However, the spectral components for the promoted systems differ from that extracted for Mo_2C/SiO_2. The latter still presents a pre-edge (Fig. S14a), as is also seen on the spectrum reported in the literature for Mo_4O_{11}, an oxide in which two Mo atoms have been reduced to Mo(V) [62]. The presence of two maxima in the derivative (Fig. S14b), close to those of the MoO_3 and MoO_2 standards, suggests the presence of several oxidation states in the oxide. In contrast, the derivatives calculated for $Ni-Mo_xC_y/SiO_2$ and $Cu-Mo_xC_y/SiO_2$ resemble more that of Mo(IV)-containing MoO_2, in line

with the position of the first three EXAFS oscillations (Fig. S14c), and with the position of the peaks on the Fourier transform (Fig. S14d). The second spectral component thus reflects the formation of Mo suboxides (average oxidation state comprised between Mo(IV) and Mo(VI) by reduction of Mo(VI).

The third spectral components (Fig. S15) share two common characteristics: the shape of the XANES spectrum, displaying on the white line a first feature more intense than the second one, similar to the spectra recently assigned to a Mo oxycarbide intermediate [39,40] (Fig. S15a); and a further decrease of the average oxidation state of Mo, with one maximum of the derivative of the XANES spectrum remaining close to that of MoO_2, and a shoulder at lower energy close to that of metallic Mo (Fig. S15b). This composite aspect is also found in the examination of the EXAFS oscillations. The position of the first oscillations roughly corresponds to those found for MoO_2, but the next ones are different (Fig. S15c). Finally, if the first peak in the Fourier transform is found at the position expected for a O shell, like in MoO_2, the second peak does not correspond to the Mo shell from MoO_2 and is located at a slightly larger distance than the first peak of Mo neighbors in metallic
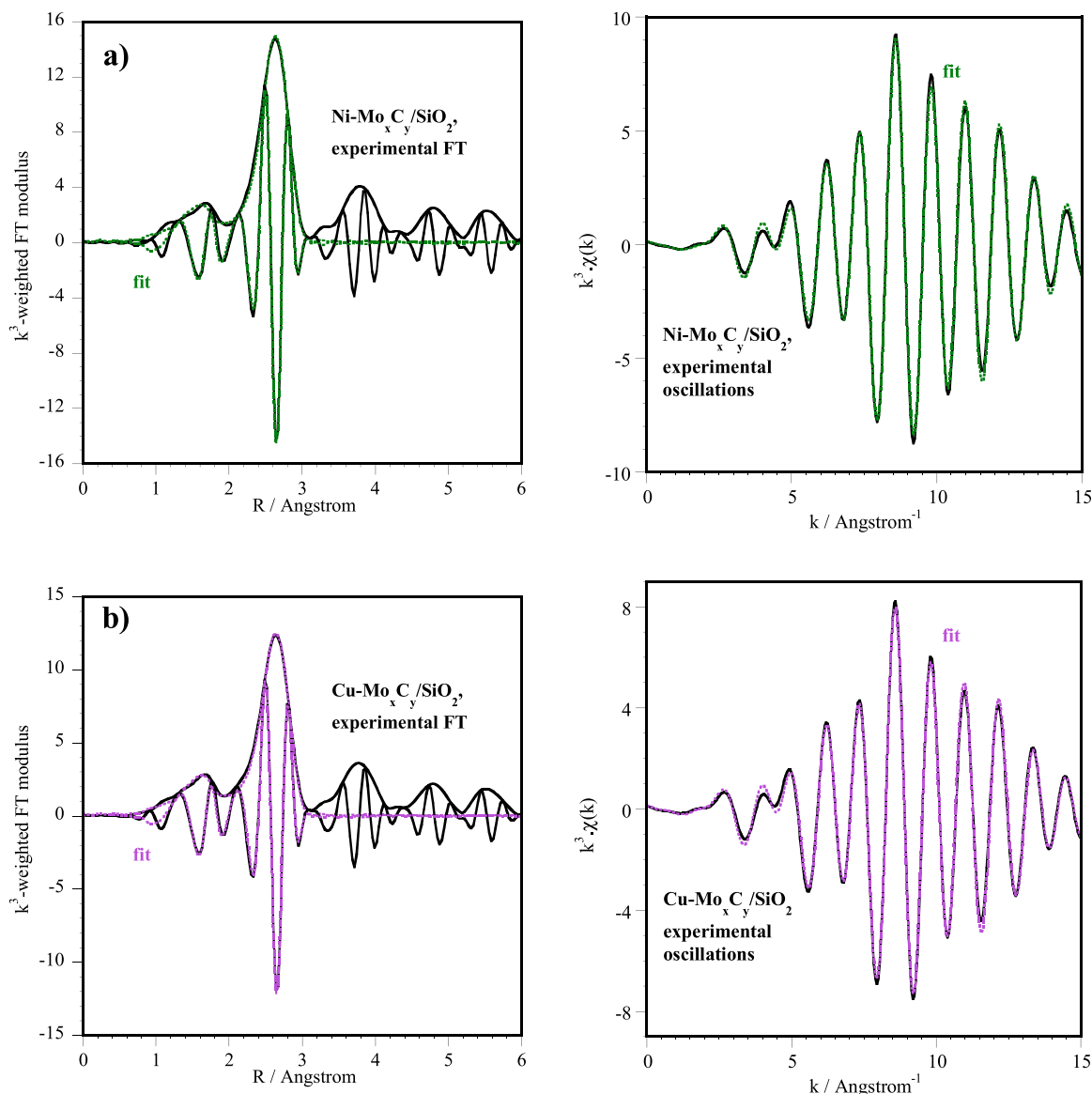
Fig. 2. XAS data at the Mo K-edge after carburization of a) Ni-Mo$_x$C$_y$/SiO$_2$ and b) Cu-Mo$_x$C$_y$/SiO$_2$ (spectra recorded at room temperature). The fit of the first and second shells of neighbors: Fourier transform (left) and EXAFS oscillations (right). k = 3.5–15 Å^{-1}.

Table 2
Fitted parameters at the Mo K-edge (E$_0$ = 20013 eV, S$_0^2$ = 0.98) were determined from the EXAFS analysis of spectra recorded at room temperature on carburized catalysts. k = 3.5–15 Å^{-1}. The fit of the first peaks from the Fourier transform is between 1 and 3 Å.

Catalyst	Backscatter	N	σ^2 (Å^2) x 10^3	R (Å)
β-Mo$_2$C[a]	C	2.7 ± 0.9	4.1 ± 0.3	2.08 ± 0.02
	Mo	7.3 ± 0.8	5.7 ± 0.5	2.966 ± 0.005
	ΔE$_0$ = −5.5 eV, r-factor = 0.01575, χ^2 = 592, N$_{ind}$ = 13, N$_{var}$ = 7			
β-Mo$_2$C/SiO$_2$	C	3.5 ± 0.9	6 ± 2	2.10 ± 0.01
	Mo	7.3 ± 0.8	7.3 ± 0.6	2.978 ± 0.005
	ΔE$_0$ = −3.8 eV, r-factor = 0.01462, χ^2 = 441, N$_{ind}$ = 13, N$_{var}$ = 7			
Ni-Mo$_x$C$_y$/SiO$_2$	C	4 ± 1	6 ± 2	2.10 ± 0.01
	Mo	7.5 ± 0.8	6.7 ± 0.5	2.979 ± 0.004
	ΔE$_0$ = −4.5 eV, r-factor = 0.01232, χ^2 = 301, N$_{ind}$ = 13, N$_{var}$ = 7			
Cu-Mo$_x$C$_y$/SiO$_2$	C	3.5 ± 0.9	6 ± 2	2.10 ± 0.01
	Mo	7.1 ± 0.8	7.2 ± 0.6	2.981 ± 0.005
	ΔE$_0$ = −4.2 eV, r-factor = 0.01481, χ^2 = 425, N$_{ind}$ = 13, N$_{var}$ = 7			

[a] (after reactivation in H$_2$ at 400 °C)

Mo (Fig. S15d).

To obtain more precise structural information on these intermediate species, the second and third spectral components extracted for Cu-Mo$_x$C$_y$/SiO$_2$ were selected for EXAFS fitting. This system was chosen because it is the one for which the intermediate spectral components appear most sequentially and are more likely to represent distinct species.

The identification of a MoO$_2$-like phase is confirmed for the second spectral component, by comparison with a fit done on the spectrum of MoO$_2$ using the same number of parameters (Table S1, Fig. S16). The only difference is a Mo-Mo interatomic distance longer by 0.07 Å.

A precise assignment is more difficult to establish for the third spectral component (Table S1, Fig. S17). The first peak in the Fourier transform is found to arise from a shell of O atoms. A fit using both C and O atoms appears less plausible, because it results in an extremely low Debye-Waller parameter, lower than that found when fitting the EXAFS signal of a well-organized oxide like MoO$_2$ at RT. The second peak corresponds to Mo neighbors at an interatomic distance of 2.80 Å, which is both larger than the Mo-Mo distance in metallic Mo (2.72 Å), and smaller than the distances evaluated in the carburized catalysts (Table 2;

approximately 2.97 Å), or in the crystalline oxycarbide phases whose structure was described in detail by Bouchy et al. [63] (2.90–2.96 Å). The high Debye-Waller factor for the second shell can be explained by a thermal effect (as will be seen below, the third component is prominent at about 400 °C) or by a structural disorder around Mo.

In a conclusion, a comparison with the spectra presented in the literature points to phases mentioned as oxycarbides MoO_xC_y. But the impossibility to fit the first shell with a combination of C and O atoms, and the Mo-Mo interatomic distance, which significantly differs from those reported either in organized oxycarbide crystals or metallic Mo, also suggests the formation of a heterogeneous, mostly oxidic, system, in which only a fraction of Mo has pursued its reduction or is initiating its carburization. It will be seen in the section dedicated to temperature-programmed carburization that the degree of carburization of this species may not be the same for the three systems.

Finally, the fourth spectral component extracted by the MCR-ALS procedure is identical to that of the final Mo carbide, as confirmed by a comparison of the position of the oscillations with those recorded after cooling under CH_4/H_2 to RT (Fig. S18). The damping is due to thermal effects.

The evolution of the spectra recorded during the carburization of Ni-Mo_xC_y/SiO_2 at the Ni K-edge is presented in Fig. S19. The initial intense white line is characteristic of Ni^{2+}, and its disappearance indicates that nickel is reduced to the metallic state during the first half of the ramp. But even after reduction, some changes in the spectra are visible (yellow-red spectra).

EXAFS confirms that in the calcined precursor, Ni^{2+} is present in the α-$NiMoO_4$ phase detected by Raman spectroscopy; NiO would provide very different oscillations (Fig. S20). The expected number of neighbors and interatomic distances in the crystal structure are 6 O atoms at R = 2.018–2.140 Å, 2 Ni atoms at R = 3.027 Å, and 2 Mo atoms at R = 3.207 Å, and correspond to those determined by fitting (Table 3). The fit was not attempted at longer distances owing to the superimposition of more than 10 multiple scattering paths between 3.4 and 4 Å.

A spectrum recorded during carburization at 400 °C is presented in Fig. S21a. As was anticipated from Fig. S19, Ni is now in a reduced, metallic state (comparison of the edge position with Ni foil, position in energy of the main oscillations, Fig. S21a and b). But the shape of the spectrum just past the edge is different from that of bulk Ni metal, with a complete absence of structuration around 8350 eV. The peak of nearest neighbors on the Fourier transform is also located at a significantly shorter distance than in metallic Ni (Fig. S21c), which may indicate that

small groups of Ni atoms, which one can presume are stabilized by an underlying Mo-based phase, have not formed well-organized metal particles yet.

In contrast, after carburization has been completed and cooling to RT has taken place (Fig. 3a and S22), face-centered (fcc) cubic Ni is detected. The number of nearest neighbors is far below the value of 12 in bulk Ni (Table 3). A value of 6.8, as found here, can be linked to small Ni particles, whose size would be close to 1 nm [64], a highly dispersed state for reduced Ni. The interatomic distance (2.494 Å) corresponds to that in metallic Ni, and the hypothesis of a Ni carbide, in which distances are longer, can be excluded (a Ni - Ni distance of 2.63 Å was reported for Ni_3C by Struis et al. [65]).

The MCR-ALS analysis of the carburization of Ni-Mo/SiO_2 at the Ni K-edge extracts three spectral components (Figs. S23–S25). The first one corresponds to $NiMoO_4$, the second one is identical to the spectrum recorded at 400 °C (small groups of Ni atoms), the third one to fcc Ni nanoparticles, with EXAFS oscillations damped because of a strong thermal effect in the last part of the temperature ramp.

The evolution of the spectra recorded during the carburization of Cu-Mo_xC_y/SiO_2 at the Cu K-edge is presented in Fig. S26. The reduction of Cu^{2+}, characterized by the intense white line, takes place at a low temperature. An intermediate species then contributes to a well-visible pre-edge feature, distinct from that of metallic Cu and more intense, before the typical spectrum of metallic Cu appears.

The analysis of the XAS data is much less informative than at the Ni K-edge. The position in the energy of the XANES spectrum recorded on the calcined system (Fig. S27) is similar to that of standard CuO, which indicates that Cu is present in the Cu^{2+} state, but the spectrum is different: for example, no pre-edge feature is present. This absence of a pre-edge feature was also reported in the literature for γ-$CuMoO_4$ [55]. The fit of the EXAFS data only reveals a shell of O atoms around Cu^{2+}, which explains why the EXAFS oscillations are seen at approximately the same energies as in CuO (Table 3). These observations remain consistent with the hypothesis of poorly organized Cu^{2+} molybdates suggested by Raman spectroscopy.

Fig. S28 presents two spectra recorded at 200 and 240 °C. At 200 °C, the position of the edge is intermediate between that of CuO and Cu_2O. However, the intense pre-edge feature and the EXAFS oscillations are different from those of these standards. In contrast, the species detected at 240 °C is metallic Cu. This is confirmed by the Fourier transform that shows the four successive peaks characteristic of the face-centered cubic metal (Fig. S29). At 200 °C, the Fourier transform presents two peaks: one at the position of O nearest-neighbors, like in Cu_2O; the second one at the position of Cu nearest-neighbors in the metal, and not in Cu_2O. XANES spectra found in the literature that display the same shape have been interpreted either as Cu_2O clusters, small partly oxidized Cu clusters, or metallic Cu clusters stabilized by ligands or by an oxidic matrix [66–74]. The position of the peaks on the Fourier transform favors the latter interpretation.

After carburization and cooling to RT, Cu is unambiguously present as fcc Cu nanoparticles (Figs. 3b and S30). The number of nearest neighbors, 9 (Table 3), shows that these nanoparticles are larger than the Ni nanoparticles detected after the carburization of Ni-Mo_xC_y/SiO_2.

The MCR-ALS analysis of the carburization ramp at the Cu K-edge provides four spectral components (Figs. S31–S34): Cu^{2+} in the initial copper molybdates; the Cu clusters in contact with an oxidic matrix; metallic fcc Cu nanoparticles; and a fourth component also representing metallic Cu (XANES spectrum), but whose Fourier transform is shifted to lower distances compared with the metal standard. Spectra recorded during the cooling of the sample show that this contribution reverts to the third spectral component in a linear way to temperature. One can thus surmise that the fourth contribution comes from a reversible thermally induced distortion of the spectrum of Cu nanoparticles. The third and fourth contributions will thus be treated as a single species, fcc Cu, in the following.

The reduction of Mo oxides and the formation of Mo carbides during

Table 3

Fitted parameters at the Ni K-edge ($E_0 = 8339 \pm 2$ eV, $S_0^2 = 0.80$) or at the Cu K-edge ($E_0 = 8987 \pm 4$ eV, $S_0^2 = 0.91$) determined from the EXAFS analysis of spectra recorded at room temperature. $k = 3–13$ Å^{-1} at the Ni K-edge, $k = 3.5–14$ Å^{-1} at the Cu K-edge. The fit of the first peak(s) from the Fourier transform between 1 and 3 Å.

Catalyst	Backscatter	N	σ^2 (Å^2) x 10^3	R (Å)
Ni-Mo_xC_y/SiO_2 calcined	O	6.4 ± 0.7	6 ± 2	2.030 ± 0.009
	Ni	1.4 ± 0.6	6 ± 2	2.97 ± 0.03
	Mo	1.6 ± 0.9	6 ± 2	3.17 ± 0.03
	r-factor = 0.01766, $\chi^2 = 365$, $N_{ind} = 12$, $N_{var} = 8$			
Ni-Mo_xC_y/SiO_2 carburized	Ni	6.8 ± 0.5	8.3 ± 0.6	2.494 ± 0.004
	r-factor = 0.00473, $\chi^2 = 427$, $N_{ind} = 12$, $N_{var} = 4$			
Cu-Mo_xC_y/SiO_2 calcined	O	4.9 ± 0.3	4.9 ± 0.6	1.941 ± 0.004
	r-factor = 0.00791, $\chi^2 = 41$, $N_{ind} = 13$, $N_{var} = 4$			
Cu-Mo_xC_y/SiO_2 carburized	Cu	9.0 ± 0.7	9.6 ± 0.6	2.544 ± 0.005
	r-factor = 0.00598, $\chi^2 = 148$, $N_{ind} = 13$, $N_{var} = 4$			
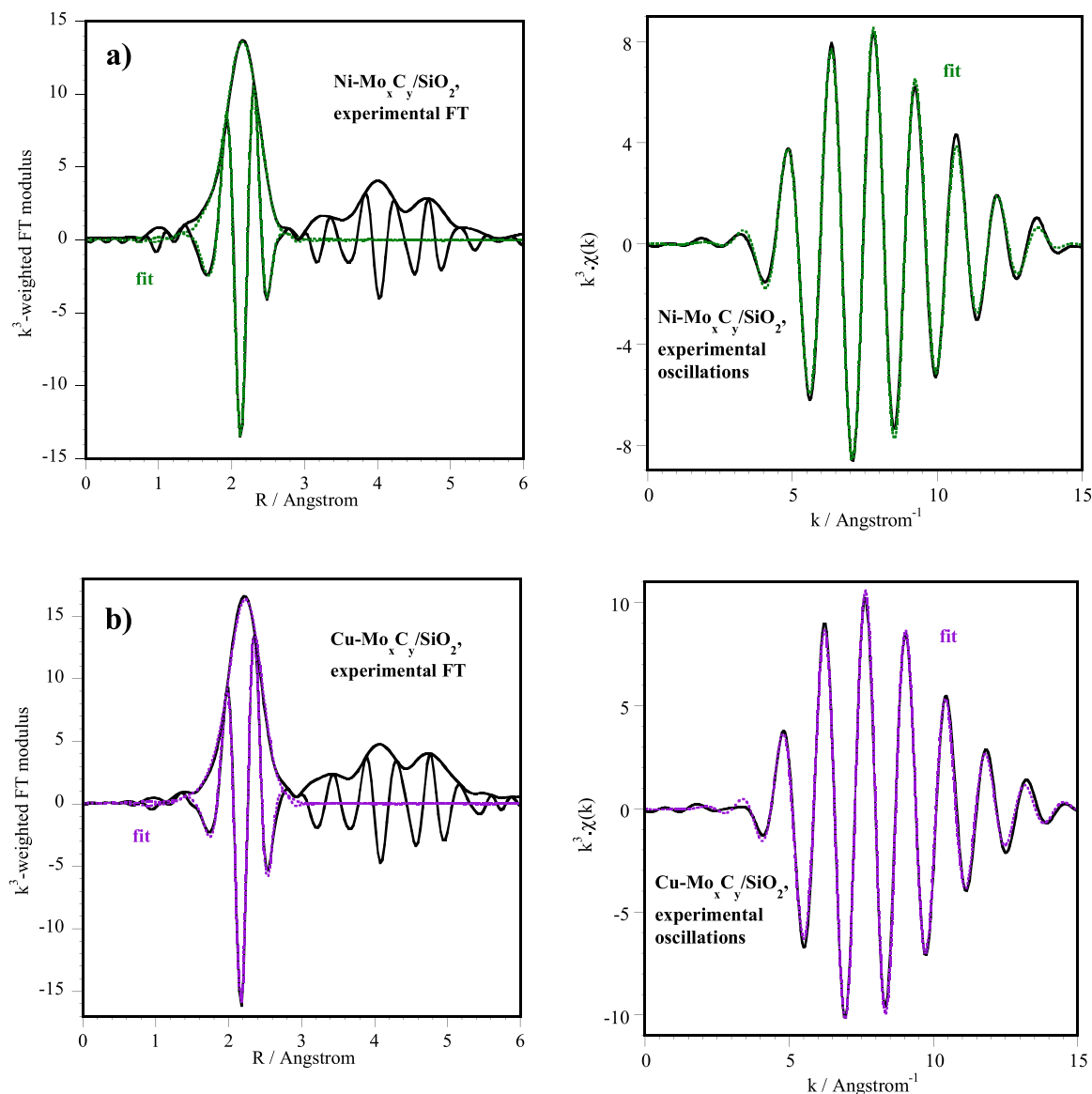
Fig. 3. XAS data of: a) Ni-Mo$_x$C$_y$/SiO$_2$ at the Ni K-edge and b) Cu-Mo$_x$C$_y$/SiO$_2$ at the Cu K-edge, after carburization (spectra recorded at room temperature). The fit of the first shell of neighbors: Fourier transform (left) and EXAFS oscillations (right), k = 3–13 Å^{-1} at the Ni K-edge, k = 3.5–14 Å^{-1} at the Cu K-edge.

carburization with CH$_4$ and H$_2$ mixture was also followed by temperature-programmed carburization in a separate experiment (Fig. 4), which revealed the associated production of water and CO.

The water signal during the carburization of the unsupported Mo$_2$C catalyst showed a maximum at 640 °C with a shoulder at 625 °C (Fig. 4). According to the literature, for the MoO$_3$ carburization taking place in an atmosphere of CH$_4$/H$_2$, the shoulder is ascribed to the reduction of MoO$_3$ to MoO$_2$, while the peak corresponds to the carburization of MoO$_2$ and formation of the Mo carbide (β-Mo$_2$C), which is followed by the consumption of methane and production of CO [38,75–77].

The thermograms of the supported catalysts, in special the bimetallic carbides, are way more complex and difficult to interpret, but the MCR-ALS analysis of the *in situ* XAS experiments sheds light on the changes in Mo, Ni, and Cu speciation taking place during the carburization. The weights of each spectral component deduced from the MCR-ALS analysis are presented as a function of temperature in Fig. 5. Each curve corresponding to the disappearance of a species, by reduction or carburization, exhibits an inflection point (maximum rate of consumption), that should correspond to a peak of water or CO production on the thermograms, allowing identification of the various stages of reaction.

By supporting the carbide on silica (Mo$_2$C/SiO$_2$ catalyst), the transformations occur at clearly lower temperatures than for the bulk carbide. The main two peaks are shifted to 400 and 550 °C. XAS suggests that the very small production of water around 300 °C corresponds to the reduction by H$_2$ of MoO$_3$ to a Mo suboxide. The very low degree of reduction could validate the hypothesis of a reduction to Mo$_4$O$_{11}$, in which the reduction of Mo(VI) to Mo(V) concerns a minor number of Mo ions. Given the overlapping domains of the predominance of the second and third components, the exact attribution of the peak at 400 °C is more difficult. It could be associated with a further reduction of Mo$_4$O$_{11}$ to the species providing the third spectral component, and minor concomitant production of CO could be linked to the starting carburization of a Mo fraction. This species is tentatively named MoO$_{(2-x)}$C$_x$, to take the further reduction of Mo into account, while distinguishing it from a bulk oxycarbide. The water production and onset of CO production at 550 °C correspond to the formation of the Mo carbide.

For the Ni-Mo$_x$C$_y$/SiO$_2$ catalyst, the peaks at 270 and 358 °C are associated with the reduction of MoO$_3$ and NiMoO$_4$, to MoO$_2$ and groups of reduced Ni atoms. The reduction of NiMoO$_4$ was indeed reported to occur in the 250–400 °C range in the literature [78]. Because of the
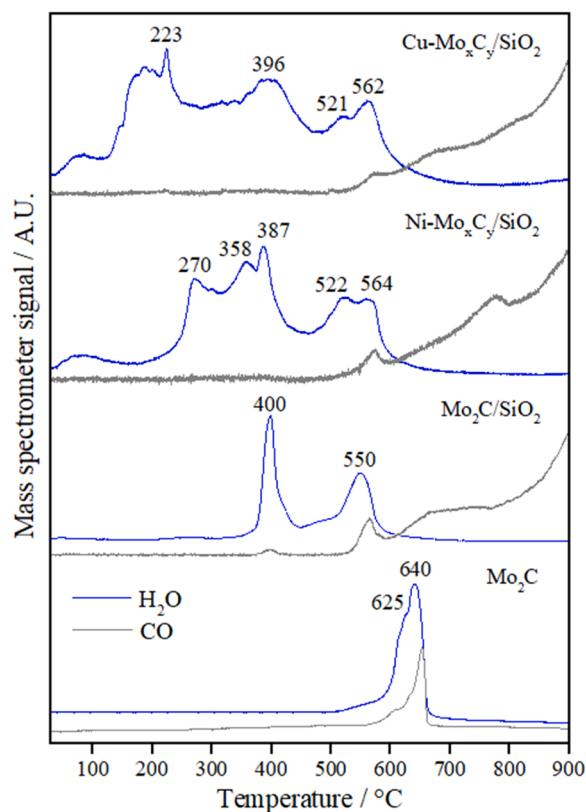
Fig. 4. Water and CO formation profiles during temperature programmed carburation of the calcined precursors of Cu-Mo$_x$C$_y$/SiO$_2$, Ni-Mo$_x$C$_y$/SiO$_2$, Mo$_2$C/SiO$_2$, and Mo$_2$C.

slightly delayed reduction of Ni^{2+} to Mo(VI), which was checked not to be an analysis artifact by comparing the experimental spectra at the Mo and Ni K-edges in the 220–250 °C range, NiMoO$_4$ seems to reduce after the reduction of MoO$_3$ has started. Compared with Mo$_2$C/SiO$_2$, there is a significant gain in reduction temperature.

The peak at 387 °C can be assigned to the reduction of MoO$_2$ to the partly reduced oxide represented by the third spectral component (MoO$_{(2-x)}$C$_x$). But in this case, the reaction is not accompanied by a release of CO and the oxide may exhibit carburization only to a very small extent. As was the case for Mo$_2$C/SiO$_2$, the final Mo carburization takes place above 500 °C, in two stages that the MCR-ALS analysis cannot explain. It is accompanied by the formation of the fcc Ni nanoparticles (NP), out of the groups of atoms presumably stabilized by the Mo phase.

For the Cu-Mo$_x$C$_y$/SiO$_2$ catalyst, the intensity of the water signal starts to increase at 120 °C and exhibits a maximum at 223 °C with several shoulders. These peaks are associated with the reduction of Cu^{2+} in the copper molybdate phases, followed by the rapid reduction of Mo (VI) oxides to MoO$_2$. Compared with the former systems, the gain in temperature for this reduction step is relevant. It may be associated with the poorly crystalline nature of the Cu molybdates and with the subsequent activation of H$_2$ on the newly-formed Cu nanoparticles in the 200–225 °C range. The next pronounced peak at 396 °C refers to the reduction of MoO$_2$ to the partly reduced oxide represented by the third spectral component, here again without production of CO, and the final stages of carburization take place above 500 °C.

In conclusion, both the TPC profiles and MCR-ALS diagrams indicate that the last steps of reduction and carburization occur in the same temperature range for the three supported catalysts. The main gain upon the addition of a promoter concerns the initial reduction of Mo(VI) oxides and can be linked to the crystallinity of the mixed molybdates, and to the temperature at which metal particles able to activate H$_2$ are
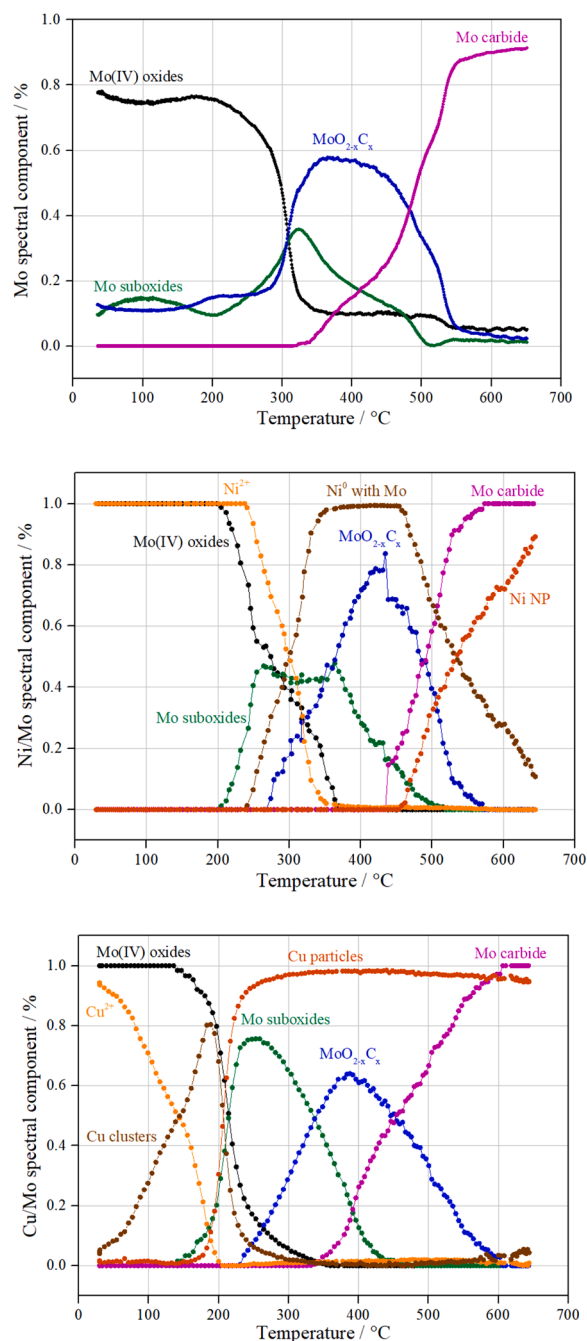

Fig. 5. Concentrations profiles of Mo, Ni, and Cu species during TPC of the calcined precursors of a) Mo$_2$C/SiO$_2$, b) Ni-Mo$_x$C$_y$/SiO$_2$, and c) Cu-Mo$_x$C$_y$/SiO$_2$ from MCR-ALS analysis of the Mo, Ni, and Cu K-edge data.

formed.

This effect has been observed before by Jung et al. [79] during the carburization of MoO$_3$ promoted with Ni, Cu, Co, Pd, and Pt under CH$_4$/H$_2$. The presence of a promoter decreased the starting temperature of the initial reduction for all materials. Similarly, Zhang et al. [80] observed by temperature programmed reduction of NiO, MoO$_3$, and NiMoO$_x$ in H$_2$ that Ni species in NiMoO$_x$ were more difficult to reduce than in NiO, while the Mo species were easily reduced in comparison with MoO$_3$.

On the other hand, the presence of Ni and Cu as promoters has been reported in the literature to favor the carburization process because these metals cause the activation and dissociation of CH$_4$ into carbon and hydrogen at lower temperatures compared with non-promoted

carbides [79,81], but this is not observed in the present work.

We also demonstrate that after completion of carburization, Ni and Cu are both present as metal nanoparticles, probably in strong stabilizing interaction with the underlying Mo carbide given their small size, but bimetallic NiMo or CuMo carbide phases were not formed. Ni nanoparticles appear more dispersed than Cu nanoparticles, and no Ni carbide is evidenced after carburization.

3.2. HDO of m-cresol over Mo carbides-based catalysts

The HDO reaction rate, distribution of products, and yield at low conversion using *m*-cresol as a model molecule are reported in Table 4. Mo_2C, Mo_2C/SiO_2, and $Ni-Mo_xC_y/SiO_2$ exhibited approximately the same HDO deoxygenation activity (mmol/g_{cat}), whereas $Cu-Mo_xC_y/SiO_2$ and Ni/SiO_2 were less active (7-fold). However, when the reaction rate is expressed per gram of Mo, it is clear that the Mo_2C/SiO_2 catalyst is 4-fold more active than Mo_2C, revealing the effect of support on improving the dispersion of Mo carbide phase.

The lower activity of the Mo carbide promoted with Cu in comparison with the Mo_2C, Mo_2C/SiO_2 and $Ni-Mo_xC_y/SiO_2$ catalysts might be associated with the presence of poorly organized Cu^{2+} molybdates species in the calcined precursor of the $Cu-Mo_xC_y/SiO_2$ catalyst as observed by Raman spectroscopy and XAS experiments. This could lead to the formation of large particle size and consequent lower dispersion of metallic Cu and Mo_2C species after carburization, as demonstrated by EXAFS experiments (Tables 2 and 3). Therefore, a lower intimate contact between Cu and Mo_2C is observed, in contrast to what is observed for the $Ni-Mo_xC_y/SiO_2$ catalyst. In this case, small Ni^0 particles were formed as evidenced by XAS studies.
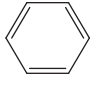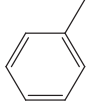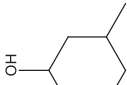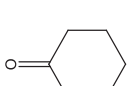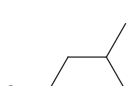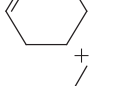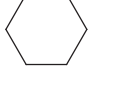
The effect of promoter on catalyst activity is more evident when comparing the reaction rates expressed per gram of Mo. The Mo_2C/SiO_2 catalyst is 5-fold more active than $Cu-Mo_xC_y/SiO_2$, whose reaction rate is similar to that one for unsupported Mo_2C. In fact, *m*-cresol was not converted over the Cu/SiO_2 catalyst and then, the lower activity of $Cu-Mo_xC_y/SiO_2$ catalyst could be attributed to the lower amount of Mo_2C phase (in comparison to Mo_2C/SiO_2) as well as the low dispersion of Mo_2C phase. Meanwhile, the presence of well-dispersed metallic Ni particles is likely responsible for the high activity of the $Ni-Mo_xC_y/SiO_2$ catalyst. However, the activity of $Ni-Mo_xC_y/SiO_2$ and $Cu-Mo_xC_y/SiO_2$ catalysts cannot be explained by the formation of a bimetallic Mo carbide phase, regardless of the type of metal promoter (Ni or Cu), because the XAS experiments showed the formation of isolated metallic Ni and Cu particles.

Regarding product distribution, toluene was the only product formed over Mo_2C, Mo_2C/SiO_2, and $Cu-Mo_xC_y/SiO_2$ catalysts after carburization at 650 °C. In addition to toluene, a small amount of *m*-cyclohexene (4.2 %) was also produced over $Ni-Mo_xC_y/SiO_2$ catalyst. On the other hand, several products were observed for Ni/SiO_2 catalyst: methane (31.1 %), methylcyclohexanone (32.3 %), toluene (20.2 %), methylcyclohexanol (7.5 %), phenol (7.0 %), and minor amounts of cyclohexanone, benzene, and methylcyclohexene. These results reveal that the Mo-carbide phase is selective to deoxygenation products.

The results of *m*-cresol conversion as a function of W/F at 300 °C over Mo_2C and $Ni-Mo_2C/SiO_2$ are shown in Fig. 6. Increasing the residence time increased *m*-cresol conversion but the product distribution remained unchanged with toluene as the main compound formed for Mo_2C (> 99 %) and $Ni-Mo_2C/SiO_2$ (95 %).

For the HDO of phenol and *m*-cresol, it has been proposed that the reaction follows a tautomerization mechanism that covers three main reaction pathways: (i) the sequential hydrogenation of the aromatic ring from the keto tautomer intermediate, producing cyclohexanone/methylcyclohexanone and cyclohexanol/methylcyclohexanol; (ii) the hydrogenation of the carbonyl group from the tautomer with the formation of unsaturated alcohol that is dehydrated to benzene/toluene; (iii) the direct deoxygenation of the tautomer, producing benzene/toluene [82–84].

Table 4
Conversion, HDO reaction rate, and selectivity for the HDO of *m*-cresol over Mo carbides catalysts at 300 °C and 1 atm.

Catalyst	Conversion (%)	W/F (g min mmol$_{cresol}^{-1}$)	Rate of HDO (mmol$_{cresol}$ g$_{Mo}^{-1}$)	Rate of HDO (mmol$_{cresol}$ g$_{cat.}^{-1}$)	Selectivity (%) CH$_4$	+	O (methylcyclohexanone)	O (cyclohexanone)	OH (methylcyclohexanol)	toluene	benzene	OH (phenol)
Mo$_2$C	14.9	0.437	0.34	0.34	-	-	-	-	-	100.0	-	-
Mo$_2$C/SiO$_2$	17.1	0.742	1.37	0.24	-	-	-	-	-	100.0	-	-
Ni-Mo$_x$C$_y$/SiO$_2$	22.7	0.734	1.93	0.31	-	4.2	-	-	-	95.8	-	-
Cu-Mo$_x$C$_y$/SiO$_2$	8.7	2.253	0.26	0.04	-	-	-	-	-	100.0	-	-
Ni/SiO$_2$	17.7	-	-	0.05	31.1	0.2	32.3	1.0	7.5	20.2	0.4	7.0
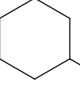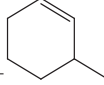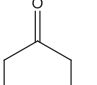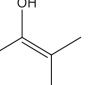
Fig. 6. The *m*-cresol conversion as a function of W/F for the HDO of *m*-cresol at 300 °C over: (a) Mo_2C; (b) $Ni-Mo_2C/SiO_2$.

Table 5
Conversion and distribution of products for the HDO of *m*-cresol over different catalysts from the literature at 300 °C and 1 atm.

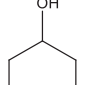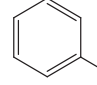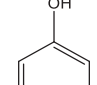| Catalyst	Conversion (%)	Selectivity (%)								Reference
		CH_4								
5 % Ni/ SiO$_2$	16.2	13.0	-	33.3	11.1	14.2	-	28.4	-	[82]
5 % Fe/ SiO$_2$	8.8	-	-	-	-	60.2	-	39.8	-	[82]
5 % Ni-5 % Fe/ SiO$_2$	13.7	2.2	-	-	-	52.6	-	45.3	-	[82]
Pt/SiO$_2$	7.2	-	-	60.2	6.5	33.3	-	-	-	[83]
Ru/SiO$_2$	4.5	43.4 (10.7)[a]	-	7.4	-	38.5	-	-	-	[83]
Pd/SBA-15	7.0	-	-	62.0	-	38.0	-	-	-	[7]
Pd/5 % Al-SBA-15	5.0	-	–	5.0	–	77.0	3.0	9.0	6.0	[7]
Pd/20 % Al-SBA-15	6.0	–	–	–	–	50.0	8.0	27.0	15.0	[7]
Pd/SiO$_2$	8.2	–	–	90.3	5.9	3.8	–	–	–	[90]
Pd/ CeO$_2$	11.5	–	–	78.4	9.9	11.7	–	–	–	[90]
Pd/ZrO$_2$	14.7	–	0.4	18.4	1.2	80.0	–	–	–	[90]
Pd/TiO$_2$	7.3	–	–	12.6	–	87.9	–	–	–	[90]
Pd/ Nb$_2$O$_5$	13.1	–	0.6	3.8	–	95.6	–	–	–	[90]

[a] C_2-C_5 hydrocarbons

In the tautomerization mechanism, the types of metal and support used affects significantly the HDO reaction pathways [5,85–89]. The hydrogenation of the ring is promoted by metals such as Pt, Pd, Ni, and Co supported by SiO_2, Al_2O_3, and CeO_2. On the other hand, the deoxygenation route is favored on oxophilic metals and supports such as Ru, Fe, ZrO_2, TiO_2, and Nb_2O_5. But, despite its high deoxygenation capacity, an oxophilic metal such as Ru also promotes the hydrogenolysis reaction of the intermediate formed, producing large amounts of methane and C_2-C_5 hydrocarbons. In the case of Fe, its incomplete reduction may produce Lewis acidic sites that catalyze alkylation reactions. Therefore, all these metals present some drawbacks in producing deoxygenated products with high selectivity.

Table 5 lists the product distribution for the HDO of *m*-cresol obtained with different catalysts from the literature [5,7,82,90]. Ni-based catalyst promotes the hydrogenolysis and the formation of methane as well as the hydrogenation of the ring with the production of methyl-cyclohexanone and methylcyclohexanol. Pd/SBA-15, Pd/SiO_2, and Pt/SiO_2 are very selective to methylcyclohexanone without methane formation. Oxophilic metals such as Ru and Fe promote the formation of toluene. Furthermore, the presence of unreduced iron (Lewis acidic site) favors the alkylation reaction and the production of xylenols and *o*-cresol. Therefore, the type of active phase used for the HDO of *m*-cresol significantly affects the product distribution. This has been previously reported in the literature for the HDO of phenol [85,87] and *m*-cresol [5]. Teles et al. [85] studied the effect of metal type on the HDO of phenol over silica-supported catalysts. They suggested that phenol is mainly tautomerized, followed by hydrogenation of the aromatic ring over Pd/SiO_2, Pt/SiO_2, and Rh/SiO_2 catalysts. Oxophilic metals such as Ru and Co promote direct deoxygenation to benzene and hydrogenolysis with the production of methane. Tan et al. [5] reported different product distribution for the HDO of *m*-cresol over Pt/SiO_2, and Ru/SiO_2 catalysts. Methylcyclohexanone was the main product formed over Pt/SiO_2, while toluene was mainly produced for Ru/SiO_2.

The different reaction pathways proposed in the literature for the HDO of *m*-cresol are represented by Scheme 1 [6,82,90,91]. The results obtained in our work suggest that the Mo-carbide phase promotes direct deoxygenation to toluene as it is observed for oxophilic metals such as Ru [5]. DFT calculations showed that the direct dehydroxylation of *m*-cresol is more favorable than the tautomerization route over the more oxophilic Ru (0001) surface. The direct dehydroxylation of *m*-cresol over Ru (0001) produces a partially unsaturated hydrocarbon surface species C_7H_7 *, which may lead to the formation of C_1-C_5 hydrogenolysis products or toluene by its hydrogenation. For Ru/SiO_2 catalyst, the C_1-C_5 hydrocarbons were the main products formed (54.1 %) [5]. In comparison to Ru, the Mo_2C phase does not produce methane, which is responsible for the higher production of toluene. This result

suggests that the Mo_2C phase promotes the hydrogenation of the unsaturated hydrocarbon surface species C_7H_7 * and suppress the formation of hydrogenolysis products.

The high selectivity to deoxygenated products of transition metal carbides for HDO reactions of different phenolic compounds has been ascribed to the high oxophilicity of the carbide phase due to the stronger adsorption of the oxygen atom from the oxygenated molecule. However, contradictory results have been reported in the literature.

The direct deoxygenation pathway was dominant on the HDO of *p*-cresol when using Mo_2C supported on activated charcoal. However, the active sites responsible for the high selectivity to deoxygenated compounds were attributed to both Mo_2C and MoO_xC_y species observed under reaction conditions depending on the catalyst interaction with oxygen atoms [19].

An almost complete selectivity to toluene was observed between 150 and 210 °C and atmospheric pressure using Mo_2C as catalyst. However, the authors demonstrated that the metal-like sites necessary for the HDO of *m*-cresol were sensitive to oxygen since the co-feed of 1 kPa of O_2 decreased the toluene synthesis rate [18].

In our work, only the deoxygenated product (toluene) was observed in the reaction over the Mo_2C, and Mo_2C/SiO_2 catalysts, indicating that Mo_2C species, detected by XAS after carburization at 650 °C, is the active site responsible for the deoxygenation of *m*-cresol. In order to confirm this proposal, the HDO of *m*-cresol reaction was carried out after the carburization of Mo_2C/SiO_2 at 400 °C. This catalyst was inactive after activation at this temperature. The MCR-ALS analysis (Fig. 5a) revealed the presence of mainly oxycarbide species ($MoO_{2-x}C_x$). Increasing the activation temperature to 650 °C completely converted $MoO_{2-x}C_x$ into Mo_2C species. Therefore, the absence of activity for Mo_2C/SiO_2 at 400 °C is likely caused by the reduction of oxophilicity due to the addition of oxygen into the molybdenum carbide structure.

The determination of the active sites for the promoted Mo carbide catalysts is more complex and it might involve: (i) the formation of bimetallic carbide phase; (ii) the presence of isolated metallic particles in close contact with the Mo carbide phase. In this last case, the metal could assist on the hydrogen activation or directly participate on the reaction mechanism.

In our work, the effect of metal promoter on product distribution of Mo_2C phase depended on the type of metal. For Ni-Mo_xC_y/SiO_2 catalyst, toluene and methylcyclohexene were the products formed. The formation of ring hydrogenation products (methylcyclohexane, methyl-cyclohexanol) for the HDO of *m*-cresol at 250 °C and 20 bar of H_2 was also observed over NiMo$_2$C/SBA-15 catalyst [32]. According to the reaction pathways of Scheme 1, *m*-cresol can be tautomerized to an intermediate that is hydrogenated to methylcyclohexanone, followed by its conversion to methylcyclohexanol. Finally, methycyclohexene is
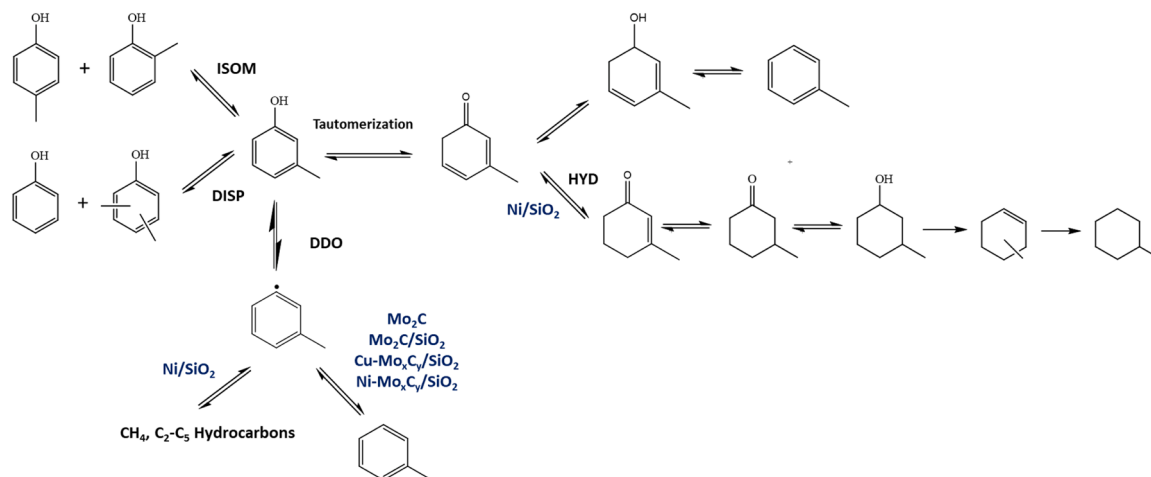
Scheme 1. Reaction scheme for the HDO of *m*-cresol [6,82,90,91].

produced through dehydration of methylcyclohexanol. Methyl-cyclohexanone and methane were the main products formed over Ni/SiO$_2$ catalyst (Table 4). This result is in agreement with the XAS experiments that demonstrated the presence of isolated metallic Ni particles, which are responsible for the hydrogenation and hydrogenolysis reactions. In addition, this result also shows that a bimetallic Ni-Mo carbide phase was not formed since no synergetic effect is observed on product distribution. The MCR-ALS analysis also did not detect the formation of a bimetallic Ni-Mo carbide phase. The deoxygenation of *m*-cresol to toluene takes place on the Mo$_2$C phase that was identified by the XAS experiments.

Cu-Mo$_x$C$_y$/SiO$_2$ exhibited the same product distribution as that observed for Mo$_2$C/SiO$_2$, which could be attributed to the absence of activity of Cu as shown by the tests with Cu/SiO$_2$ catalyst. In fact, XAS results revealed that Cu is also present as isolated metallic particles, and bimetallic Cu-Mo carbide species were not formed. Since Cu was not active for the HDO reaction, it does not affect the product distribution of Mo$_2$C.

4. Conclusions

The carburization of a monometallic (Mo$_2$C/SiO$_2$) and bimetallic Mo carbides (Ni-Mo$_x$C$_y$/SiO$_2$ and Cu-Mo$_x$C$_y$/SiO$_2$) Mo carbides under a CH$_4$/H$_2$ mixture was investigated by XAS and multivariate analysis of the spectra as a function of temperature. It was demonstrated that four successive groups of Mo species were involved in the carburization process: (i) MoO$_3$ for Mo$_2$C/SiO$_2$, and a mixture of MoO$_3$ and Ni/Cu-Mo (VI) molybdates for Ni-Mo$_x$C$_y$/SiO$_2$ and Cu-Mo$_x$C$_y$/SiO$_2$, representing the Mo(VI) oxides present on the calcined precursors; (ii) Mo$_4$O$_{11}$ (Mo$_2$C/SiO$_2$) and MoO$_2$ (Ni-Mo$_x$C$_y$/SiO$_2$ and Cu-Mo$_x$C$_y$/SiO$_2$) for Mo suboxides (oxidation state between IV and VI) formed by reduction of the Mo(VI) oxides; (iii) MoO$_{2-x}$C$_x$ formed by reduction of the Mo suboxides and characterized by a limited degree of carburization (low production of CO); (iv) Mo$_2$C formed by the full carburization of MoO$_{2-x}$C$_x$ (important production of CO).

TPC analysis was performed and compared to the XAS experiments. The synthesis of the monometallic carbide (Mo$_2$C/SiO$_2$) proceeded by the reduction of MoO$_3$ species in the calcined precursor in the range of 300–400 °C and the Mo$_2$C phase was formed above 500 °C.

Regarding the bimetallic carbides, the results showed that the reduction of the Cu molybdates present in the calcined precursor of the Cu-Mo$_x$C$_y$/SiO$_2$ catalyst started at lower temperatures in comparison with Mo species in the monometallic carbide. The produced metallic Cu particles assisted the initial reduction of the Mo species in the Cu-promoted Mo carbide by providing more hydrogen.

On the other hand, Ni molybdates found in the calcined precursor of the Ni-Mo$_x$C$_y$/SiO$_2$ catalyst were reduced at higher temperatures than the Mo species and did not contribute to the first step of reduction. No bimetallic NiMo or CuMo carbide phases were formed and Ni and Cu were found only as nanoparticles in contact with the carbide phase. Finally, both metals did not assist in the formation of the Mo$_2$C phase at higher temperatures, which occurred at the same range of temperature as observed for the monometallic Mo$_2$C/SiO$_2$ catalyst.

An unsupported and the SiO$_2$-supported Mo carbides were evaluated for the HDO of *m*-cresol in the gas phase at 300 °C and atmospheric pressure. For Mo$_2$C, Mo$_2$C/SiO$_2$, and Cu-Mo$_x$C$_y$/SiO$_2$ catalysts, only the deoxygenated product (toluene) was produced. A slightly lower formation of toluene (96 %) was observed for the Mo carbide promoted with Ni, which also followed the hydrogenation route producing methylcyclohexene due to the presence of metallic Ni particles ascertained by XAS. For Ni/SiO$_2$ catalyst, a high formation of hydrogenolysis and hydrogenation products was observed. These results demonstrate that Mo$_2$C phase detected by XAS is the active site responsible for the deoxygenation of ~~m~~*m*-cresol to toluene. However, after carburization at 400 °C, the Mo$_2$C/SiO$_2$ catalyst did not exhibit any activity, which indicates that oxycarbide species (MoO$_{2-x}$C$_x$) detected by XAS at this temperature are not active for deoxygenation. This result is likely due to the reduction in oxophilicity of the catalyst caused by the addition of oxygen to the carbide structure.

The comparison of the catalytic performance of the Mo carbides with noble-metal-based catalysts in the literature under iso-conversion of *m*-cresol proved the high selectivity of carbides to promote the formation of deoxygenated compounds.

CRediT authorship contribution statement

Leticia F. Sosa: Methodology, Formal analysis, Investigation, Visualization, and Writing - original draft. **Priscilla M. de Souza:** Methodology, Formal analysis, Investigation and Visualization. **Raphaela A. Rafael:** Methodology, Formal analysis, Investigation and Visualization. **Lucas R. Francisco:** Methodology, Formal analysis, Investigation and Visualization. **Raimundo C. Rabelo-Neto:** Methodology, Formal analysis, Investigation, Visualization, Writing - original draft. **Robert Wojcieszak:** Funding acquisition, Writing - review & editing. **Valérie Briois**: Conceptualization, Methodology, Formal analysis, Investigation, Writing - review & editing. **Eric Marceau**: Conceptualization, Methodology, Formal analysis, Investigation, Writing - original draft, Writing - review & editing. **Sébastien Paul:** Conceptualization, Methodology, Resources, Writing - review & editing, Supervision, Project administration, Funding acquisition. **Fabio S. Toniolo:** Conceptualization, Methodology, Resources, Writing - review & editing, Supervision, Project administration, Funding acquisition. **Fabio B. Noronha:** Conceptualization, Methodology, Resources, Writing - original draft, Writing - review & editing, Supervision, Project administration, Funding acquisition.

Declaration of Competing Interest

The authors declare that they have no known competing financial interests or personal relationships that could have appeared to influence the work reported in this paper.

Data Availability

Data will be made available on request.

Acknowledgments

Appendix A. Supporting information

Supplementary data associated with this article can be found in the online version at doi:10.1016/j.apcatb.2023.122720.

References

[1] J.A. Okolie, S. Nanda, A.K. Dalai, J.A. Kozinski, Chemistry and specialty industrial applications of lignocellulosic biomass, Waste Biomass. Valor 12 (2021) 2145–2169, https://doi.org/10.1007/s12649-020-01123-0.

[2] J. Zhang, J. Sun, Y. Wang, Recent advances in the selective catalytic hydrodeoxygenation of lignin-derived oxygenates to arenes, Green. Chem. 22 (2020) 1072–1098, https://doi.org/10.1039/C9GC02762A.

[3] R. Shu, R. Li, B. Lin, C. Wang, Z. Cheng, Y. Chen, A review on the catalytic hydrodeoxygenation of lignin-derived phenolic compounds and the conversion of raw lignin to hydrocarbon liquid fuels, Biomass. Bioenergy 132 (2020), 105432, https://doi.org/10.1016/j.biombioe.2019.105432.

[4] A.J.R. Hensley, Y. Wang, J.-S. McEwen, Phenol deoxygenation mechanisms on Fe (110) and Pd(111, ACS Catal. 5 (2015) 523–536, https://doi.org/10.1021/cs501403w.

[5] Q. Tan, G. Wang, L. Nie, A. Dinse, C. Buda, J. Shabaker, D.E. Resasco, Different product distributions and mechanistic aspects of the hydrodeoxygenation of m-cresol over platinum and ruthenium catalysts, ACS Catal. (2015) 13.

[6] C.A. Teles, P.M. de Souza, R.C. Rabelo-Neto, M.B. Griffin, C. Mukarakate, K. A. Orton, D.E. Resasco, F.B. Noronha, Catalytic upgrading of biomass pyrolysis vapors and model compounds using niobia supported Pd catalyst, Appl. Catal. B: Environ. 238 (2018) 38–50, https://doi.org/10.1016/j.apcatb.2018.06.073.

[7] C.A. Teles, P.M. de Souza, R.C. Rabelo-Neto, A. Teran, G. Jacobs, C. Vilela Weikert, Z.M. Magriotis, V.O.O. Gonçalves, D.E. Resasco, F.B. Noronha, Reaction pathways for the HDO of guaiacol over supported Pd catalysts: effect of support type in the deoxygenation of hydroxyl and methoxy groups, Mol. Catal. 523 (2022) 111491, https://doi.org/10.1016/j.mcat.2021.111491.

[8] K.J. Smith, Metal carbides, phosphides, and nitrides for biomass conversion, Curr. Opin. Green. Sustain. Chem. 22 (2020) 47–53, https://doi.org/10.1016/j.cogsc.2019.11.008.

[9] M. Zhou, H.A. Doan, L.A. Curtiss, R.S. Assary, Identification of active metal carbide and nitride catalytic facets for hydrodeoxygenation reactions, J. Phys. Chem. C. 125 (2021) 8630–8637, https://doi.org/10.1021/acs.jpcc.1c02387.

[10] M.M. Sullivan, C.-J. Chen, A. Bhan, Catalytic deoxygenation on transition metal carbide catalysts, Catal. Sci. Technol. 6 (2016) 602–616, https://doi.org/10.1039/C5CY01665G.

[11] Y. Han, M. Gholizadeh, C.-C. Tran, S. Kaliaguine, C.-Z. Li, M. Olarte, M. Garcia-Perez, Hydrotreatment of pyrolysis bio-oil: a review, Fuel Process. Technol. 195 (2019), 106140, https://doi.org/10.1016/j.fuproc.2019.106140.

[12] M. López, D. Hernández, J. Laverde, S. Pérez, D. López, Catalytic upgrading of residual biomass derived bio-oil over molybdenum carbide, Waste Biomass-.-. Valor 11 (2020) 2849–2856, https://doi.org/10.1007/s12649-019-00586-0.

[13] J.-S. Choi, A.H. Zacher, H. Wang, M.V. Olarte, B.L. Armstrong, H.M. Meyer, I. I. Soykal, V. Schwartz, Molybdenum carbides, active and in situ regenerable catalysts in hydroprocessing of fast pyrolysis bio-oil, Energy Fuels 30 (2016) 5016–5026, https://doi.org/10.1021/acs.energyfuels.6b00937.

[14] M. Grilc, G. Veryasov, B. Likozar, A. Jesih, J. Levec, Hydrodeoxygenation of solvolysed lignocellulosic biomass by unsupported MoS2, MoO2, Mo2C and WS2 catalysts, Appl. Catal. B: Environ. 163 (2015) 467–477, https://doi.org/10.1016/j.apcatb.2014.08.032.

[15] S. Boullosa-Eiras, R. Lødeng, H. Bergem, M. Stöcker, L. Hannevold, E.A. Blekkan, Catalytic hydrodeoxygenation (HDO) of phenol over supported molybdenum carbide, nitride, phosphide and oxide catalysts, Catal. Today 223 (2014) 44–53, https://doi.org/10.1016/j.cattod.2013.09.044.

[16] C.-J. Chen, W.-S. Lee, A. Bhan, Mo2C catalyzed vapor phase hydrodeoxygenation of lignin-derived phenolic compound mixtures to aromatics under ambient pressure, Appl. Catal. A: Gen. 510 (2016) 42–48, https://doi.org/10.1016/j.apcata.2015.10.043.

[17] D.J. Rensel, S. Rouvimov, M.E. Gin, J.C. Hicks, Highly selective bimetallic FeMoP catalyst for C–O bond cleavage of aryl ethers, J. Catal. 305 (2013) 256–263, https://doi.org/10.1016/j.jcat.2013.05.026.

[18] C.-J. Chen, A. Bhan, Mo$_2$C modification by CO$_2$, H$_2$O, and O$_2$: effects of oxygen content and oxygen source on rates and selectivity of m-cresol hydrodeoxygenation, ACS Catal. 7 (2017) 1113–1122, https://doi.org/10.1021/acscatal.6b02762.

[19] H. Wang, S. Liu, K.J. Smith, Synthesis and hydrodeoxygenation activity of carbon supported molybdenum carbide and oxycarbide catalysts, Energy Fuels 30 (2016) 6039–6049, https://doi.org/10.1021/acs.energyfuels.6b01032.

[20] W.-S. Lee, A. Kumar, Z. Wang, A. Bhan, Chemical titration and transient kinetic studies of site requirements in Mo2C-catalyzed vapor phase anisole hydrodeoxygenation, ACS Catal. 5 (2015) 4104–4114, https://doi.org/10.1021/acscatal.5b00713.

[21] W.-S. Lee, Z. Wang, R.J. Wu, A. Bhan, Selective vapor-phase hydrodeoxygenation of anisole to benzene on molybdenum carbide catalysts, J. Catal. 319 (2014) 44–53, https://doi.org/10.1016/j.jcat.2014.07.025.

[22] Q. Lu, C.-J. Chen, W. Luc, J.G. Chen, A. Bhan, F. Jiao, Ordered mesoporous metal carbides with enhanced anisole hydrodeoxygenation selectivity, ACS Catal. 6 (2016) 3506–3514, https://doi.org/10.1021/acscatal.6b00303.

[23] A.A. Smirnov, Zh Geng, S.A. Khromova, S.G. Zavarukhin, O.A. Bulavchenko, A. A. Saraev, V.V. Kaichev, D.Yu Ermakov, V.A. Yakovlev, Nickel molybdenum carbides: synthesis, characterization, and catalytic activity in hydrodeoxygenation of anisole and ethyl caprate, J. Catal. 354 (2017) 61–77, https://doi.org/10.1016/j.jcat.2017.07.009.

[24] T. Iida, M. Shetty, K. Murugappan, Z. Wang, K. Ohara, T. Wakihara, Y. Román-Leshkov, Encapsulation of molybdenum carbide nanoclusters inside zeolite micropores enables synergistic bifunctional catalysis for anisole hydrodeoxygenation, ACS Catal. 7 (2017) 8147–8151, https://doi.org/10.1021/acscatal.7b03175.

[25] A.L. Jongerius, R.W. Gosselink, J. Dijkstra, J.H. Bitter, P.C.A. Bruijnincx, B. M. Weckhuysen, Carbon nanofiber supported transition-metal carbide catalysts for the hydrodeoxygenation of guaiacol, ChemCatChem 5 (2013) 2964–2972, https://doi.org/10.1002/cctc.201300280.

[26] E. Ochoa, D. Torres, J.L. Pinilla, I. Suelves, Nanostructured carbon material effect on the synthesis of carbon-supported molybdenum carbide catalysts for guaiacol hydrodeoxygenation, Energies 13 (2020) 1189, https://doi.org/10.3390/en13051189.

[27] E. Ochoa, D. Torres, J.L. Pinilla, I. Suelves, On the hydrothermal-enhanced synthesis of highly selective Mo2C catalysts to fully deoxygenated products in the guaiacol HDO reaction, J. Environ. Chem. Eng. 9 (2021), 105146, https://doi.org/10.1016/j.jece.2021.105146.

[28] E. Blanco, C. Sepulveda, K. Cruces, J.L. García-Fierro, I.T. Ghampson, N. Escalona, Conversion of guaiacol over metal carbides supported on activated carbon catalysts, Catal. Today 356 (2020) 376–383, https://doi.org/10.1016/j.cattod.2019.08.029.

[29] S. Liu, H. Wang, K.J. Smith, C.S. Kim, Hydrodeoxygenation of 2-methoxyphenol over Ru, Pd, and Mo2C catalysts supported on carbon, Energy Fuels 31 (2017) 6378–6388, https://doi.org/10.1021/acs.energyfuels.7b00452.

[30] F.G. Baddour, V.A. Witte, C.P. Nash, M.B. Griffin, D.A. Ruddy, J.A. Schaidle, Late-transition-metal-modified β-Mo2C catalysts for enhanced hydrogenation during guaiacol deoxygenation, ACS Sustain. Chem. Eng. 5 (2017) 11433–11439, https://doi.org/10.1021/acssuschemeng.7b02544.

[31] C.-C. Tran, O. Mohan, A. Banerjee, S.H. Mushrif, S. Kaliaguine, A combined experimental and dft investigation of selective hydrodeoxygenation of guaiacol over bimetallic carbides, Energy Fuels 34 (2020) 16265–16273, https://doi.org/10.1021/acs.energyfuels.0c03102.

[32] T. Zhang, X. Guo, Z. Zhao, Glucose-assisted preparation of a nickel–molybdenum carbide bimetallic catalyst for chemoselective hydrogenation of nitroaromatics and hydrodeoxygenation of m-cresol, ACS Appl. Nano Mater. 1 (2018) 3579–3589, https://doi.org/10.1021/acsanm.8b00735.

[33] C.-C. Tran, Y. Han, M. Garcia-Perez, S. Kaliaguine, Synergistic effect of Mo–W carbides on selective hydrodeoxygenation of guaiacol to oxygen-free aromatic hydrocarbons, Catal. Sci. Technol. 9 (2019) 1387–1397, https://doi.org/10.1039/C8CY02184H.

[34] A.B. Dongil, Q. Zhang, L. Pastor-Pérez, T. Ramírez-Reina, A. Guerrero-Ruiz, I. Rodríguez-Ramos, Effect of Cu and Cs in the β-Mo2C system for CO$_2$ hydrogenation to methanol, Catalysts 10 (2020) 1213, https://doi.org/10.3390/catal10101213.

[35] X. Liu, Y. Song, W. Geng, H. Li, L. Xiao, W. Wu, Cu-Mo2C/MCM-41: an efficient catalyst for the selective synthesis of methanol from CO$_2$, Catalysts 6 (2016) 75, https://doi.org/10.3390/catal6050075.

[36] Y. Liu, J. Ding, J. Bi, Y. Sun, J. Zhang, K. Liu, F. Kong, H. Xiao, J. Chen, Effect of Cu-doping on the structure and performance of molybdenum carbide catalyst for low-temperature hydrogenation of dimethyl oxalate to ethanol, Appl. Catal. A: Gen. 529 (2017) 143–155, https://doi.org/10.1016/j.apcata.2016.11.009.

[37] J. Pang, J. Sun, M. Zheng, H. Li, Y. Wang, T. Zhang, Transition metal carbide catalysts for biomass conversion: a review, Appl. Catal. B: Environ. 254 (2019) 510–522, https://doi.org/10.1016/j.apcatb.2019.05.034.

[38] J. Lee, Molybdenum carbide catalysts I. synthesis of unsupported powders, J. Catal. 106 (1987) 125–133, https://doi.org/10.1016/0021-9517(87)90218-1.

[39] A. Kurlov, X. Huang, E.B. Deeva, P.M. Abdala, A. Fedorov, C.R. Müller, Molybdenum carbide and oxycarbide from carbon-supported MoO$_3$ nanosheets: phase evolution and DRM catalytic activity assessed by TEM and in situ XANES/XRD methods, Nanoscale 12 (2020) 13086–13094, https://doi.org/10.1039/D0NR02908D.

[40] Y. Zheng, Y. Tang, J.R. Gallagher, J. Gao, J.T. Miller, I.E. Wachs, S.G. Podkolzin, Molybdenum oxide, oxycarbide, and carbide: controlling the dynamic composition, size, and catalytic activity of zeolite-supported nanostructures, J. Phys. Chem. C. 123 (2019) 22281–22292, https://doi.org/10.1021/acs.jpcc.9b05449.

[41] J. Zhu, E.A. Uslamin, N. Kosinov, E.J.M. Hensen, Tuning the reactivity of molybdenum (oxy)carbide catalysts by the carburization degree: CO$_2$ reduction and anisole hydrodeoxygenation, Catal. Sci. Technol. 10 (2020) 3635–3645, https://doi.org/10.1039/D0CY00484G.

[42] J.A. Schaidle, N.M. Schweitzer, O.T. Ajenifujah, L.T. Thompson, On the preparation of molybdenum carbide-supported metal catalysts, J. Catal. 289 (2012) 210–217, https://doi.org/10.1016/j.jcat.2012.02.012.

[43] A.A. Smirnov, I.N. Shilov, A.A. Saraev, V.V. Kauchev, O.A. Bulavchenko, S. G. Zavarukhin, V.A. Yakovlev, Hydrogenation of furfural to 2-methylfuran over Ni-Mo2C/γ-Al2O3 catalyst, WSEAS Trans. Environ. Dev. 15 (2019) 189–196.

[44] L.A. Sousa, J.L. Zotin, V. Teixeira da Silva, Hydrotreatment of sunflower oil using supported molybdenum carbide, Appl. Catal. A: Gen. 449 (2012) 105–111, https://doi.org/10.1016/j.apcata.2012.09.030.

[45] V. Briois, C. La Fontaine, S. Belin, L. Barthe, T. Moreno, V. Pinty, A. Carcy, R. Girardot, E. Fonda, ROCK: the new Quick-EXAFS beamline at SOLEIL, J. Phys.: Conf. Ser. 712 (2016) 012149, https://doi.org/10.1088/1742-6596/712/1/012149.

[46] C. La Fontaine, L. Barthe, A. Rochet, V. Briois, X-ray absorption spectroscopy and heterogeneous catalysis: performances at the SOLEIL's SAMBA beamline, Catal. Today 205 (2013) 148–158, https://doi.org/10.1016/j.cattod.2012.09.032.

[47] C. Lesage, E. Devers, C. Legens, G. Fernandes, O. Roudenko, V. Briois, High pressure cell for edge jumping X-ray absorption spectroscopy: applications to

industrial liquid sulfidation of hydrotreatment catalysts, Catal. Today 336 (2019) 63–73, https://doi.org/10.1016/j.cattod.2019.01.081.

[48] B. Ravel, M. Newville, *ATHENA, ARTEMIS, HEPHAESTUS*: data analysis for X-ray absorption spectroscopy using *IFEFFIT*, J. Synchrotron Rad. 12 (2005) 537–541, https://doi.org/10.1107/S0909049505012719.

[49] M. Newville, *IFEFFIT*: interactive XAFS analysis and *FEFF* fitting, J. Synchrotron Rad. 8 (2001) 322–324, https://doi.org/10.1107/S0909049500016964.

[50] J. Jaumot, A. de Juan, R. Tauler, MCR-ALS GUI 2.0: new features and applications, Chemom. Intell. Lab. Syst. 140 (2015) 1–12, https://doi.org/10.1016/j.chemolab.2014.10.003.

[51] W.H. Cassinelli, L. Martins, A.R. Passos, S.H. Pulcinelli, C.V. Santilli, A. Rochet, V. Briois, Multivariate curve resolution analysis applied to time-resolved synchrotron X-ray absorption spectroscopy monitoring of the activation of copper alumina catalyst, Catal. Today 229 (2014) 114–122, https://doi.org/10.1016/j.cattod.2013.10.077.

[52] J. Hong, E. Marceau, A.Y. Khodakov, L. Gaberová, A. Griboval-Constant, J.-S. Girardon, C.L. Fontaine, V. Briois, Speciation of ruthenium as a reduction promoter of silica-supported Co Catalysts: a time-resolved in situ XAS investigation, ACS Catal. 5 (2015) 1273–1282, https://doi.org/10.1021/cs501799p.

[53] L. de Oliveira, K. Bouchmella, A. Picco, L. Capeletti, K. Gonçalves, J.H. dos Santos, J. Kobarg, M. Cardoso, Tailored silica nanoparticles surface to increase drug load and enhance bactericidal response, J. Braz. Chem. Soc. (2017), https://doi.org/10.21577/0103-5053.20170017.

[54] M. Thommes, K. Kaneko, A.V. Neimark, J.P. Olivier, F. Rodriguez-Reinoso, J. Rouquerol, K.S.W. Sing, Physisorption of gases, with special reference to the evaluation of surface area and pore size distribution (IUPAC Technical Report), Pure Appl. Chem. 87 (2015) 1051–1069, https://doi.org/10.1515/pac-2014-1117.

[55] I. Jonane, A. Cintins, A. Kalinko, R. Chernikov, A. Kuzmin, X-ray absorption near edge spectroscopy of thermochromic phase transition in CuMoO₄, Low. Temp. Phys. 44 (2018) 434–437, https://doi.org/10.1063/1.5034155.

[56] T. Mo, J. Xu, Y. Yang, Y. Li, Effect of carburization protocols on molybdenum carbide synthesis and study on its performance in CO hydrogenation, Catal. Today 261 (2016) 101–115, https://doi.org/10.1016/j.cattod.2015.07.014.

[57] H.M. Abdel-Dayem, Dynamic phenomena during reduction of α-NiMoO₄ in different atmospheres: in-situ thermo-raman spectroscopy study, Ind. Eng. Chem. Res. 46 (2007) 2466–2472, https://doi.org/10.1021/ie0613467.

[58] H. Ehrenberg, I. Svoboda, G. Witscheck, M. Wiesmann, F. Trouw, H. Weitzel, H. Fuess, J. Magn. Magn. Mater. 150 (1995) 371–376, https://doi.org/10.1016/0304-8853(95)00290-1.

[59] N. Joseph, J. Varghese, T. Siponkoski, M. Teirikangas, M.T. Sebastian, H. Jantunen, Glass-free CuMoO₄ ceramic with excellent dielectric and thermal properties for ultralow temperature cofired ceramic applications, ACS Sustain. Chem. Eng. 4 (2016) 5632–5639, https://doi.org/10.1021/acssuschemeng.6b01537.

[60] W. Tan, J. Luan, Investigation into the synthesis conditions of CuMoO₄ by an *in situ* method and its photocatalytic properties under visible light irradiation, RSC Adv. 10 (2020) 9745–9759, https://doi.org/10.1039/D0RA00496K.

[61] B. Saravanakumar, G. Ravi, R. Yuvakkumar, V. Ganesh, R.K. Guduru, Synthesis of polyoxometalates, copper molybdate (Cu₃Mo₂O₉) nanopowders, for energy storage applications, Mater. Sci. Semicond. Process. 93 (2019) 164–172, https://doi.org/10.1016/j.mssp.2019.01.002.

[62] T. Ressler, R.E. Jentoft, J. Wienold, M.M. Günter, O. Timpe, In Situ XAS and XRD Studies on the Formation of Mo Suboxides during Reduction of MoO₃, J. Phys. Chem. B 104 (2000) 6360–6370, https://doi.org/10.1021/jp000690t.

[63] C. Bouchy, I. Schmidt, J.R. Anderson, C.J.H. Jacobsen, E.G. Derouane, S.B. D. Hamid, Metastable fcc α-MoC supported on HZSM5 - preparation and catalytic performance for the non-oxidative conversion of methane to aromatic compounds, J. Mol. Catal. A: Chem. 163 (2000) 283–296.

[64] B.D. Patterson, R. Abela, Novel opportunities for time-resolved absorption spectroscopy at the X-ray free electron laser, Phys. Chem. Chem. Phys. 12 (2010) 5647, https://doi.org/10.1039/c003406a.

[65] R.P.W.J. Struis, D. Bachelin, C. Ludwig, A. Wokaun, Studying the Formation of Ni₃C from CO and Metallic Ni at *T* = 265 °C in Situ Using Ni K-Edge X-ray Absorption Spectroscopy, J. Phys. Chem. C. 113 (2009) 2443–2451, https://doi.org/10.1021/jp809409c.

[66] H. Oyanagi, Z.H. Sun, Y. Jiang, M. Uehara, H. Nakamura, K. Yamashita, Y. Orimoto, L. Zhang, C. Lee, A. Fukano, H. Maeda, Small copper clusters studied by x-ray absorption near-edge structure, J. Appl. Phys. 111 (2012), 084315, https://doi.org/10.1063/1.3700346.

[67] S. Huseyinova, J. Blanco, F.G. Requejo, J.M. Ramallo-López, M.C. Blanco, D. Buceta, M.A. López-Quintela, Synthesis of highly stable surfactant-free Cu₅ clusters in water, J. Phys. Chem. C 120 (2016) 15902–15908, https://doi.org/10.1021/acs.jpcc.5b12227.

[68] N. Mammen, L. Spanu, E.C. Tyo, B. Yang, A. Halder, S. Seifert, M.J. Pellin, S. Vajda, S. Narasimhan, Using first principles calculations to interpret XANES experiments: extracting the size-dependence of the (*p*, *T*) phase diagram of sub-nanometer Cu clusters in an O₂ environment, J. Phys.: Condens. Matter 31 (2019), 144002, https://doi.org/10.1088/1361-648X/aafcf9.

[69] N. Mammen, L. Spanu, E.C. Tyo, B. Yang, A. Halder, S. Seifert, M.J. Pellin, S. Vajda, S. Narasimhan, Reversing size-dependent trends in the oxidation of copper clusters through support effects, Eur. J. Inorg. Chem. 2018 (2018) 16–22, https://doi.org/10.1002/ejic.201701355.

[70] C. Nayak, D. Bhattacharyya, S.N. Jha, N.K. Sahoo, In situ XAS study on growth of PVP-stabilized Cu nanoparticles, ChemistrySelect 3 (2018) 7370–7377, https://doi.org/10.1002/slct.201801358.

[71] Y. Liu, N. Marcella, J. Timoshenko, A. Halder, B. Yang, L. Kolipaka, MichaelJ. Pellin, S. Seifert, S. Vajda, P. Liu, A.I. Frenkel, Mapping XANES spectra on structural descriptors of copper oxide clusters using supervised machine learning, J. Chem. Phys. 151 (2019) 164201, https://doi.org/10.1063/1.5126597.

[72] B. Zandkarimi, G. Sun, A. Halder, S. Seifert, S. Vajda, P. Sautet, A.N. Alexandrova, Interpreting the operando XANES of surface-supported subnanometer clusters: when fluxionality, oxidation state, and size effect fight, J. Phys. Chem. C 124 (2020) 10057–10066, https://doi.org/10.1021/acs.jpcc.0c02823.

[73] A. Halder, C. Lenardi, J. Timoshenko, A. Mravak, B. Yang, L.K. Kolipaka, C. Piazzoni, S. Seifert, V. Bonačić-Koutecký, A.I. Frenkel, P. Milani, S. Vajda, CO₂ Methanation on Cu-Cluster decorated zirconia supports with different morphology: a combined experimental in situ GIXANES/GISAXS, ex situ XPS and theoretical DFT study, ACS Catal. 11 (2021) 6210–6224, https://doi.org/10.1021/acscatal.0c05029.

[74] A.A. Dubale, C.-J. Pan, A.G. Tamirat, H.-M. Chen, W.-N. Su, C.-H. Chen, J. Rick, D. W. Dubale, B.A. Aragaw, J.-F. Lee, Y.-W. Yang, B.-J. Hwang, Heterostructured Cu₂O/CuO decorated with nickel as a highly efficient photocathode for photoelectrochemical water reduction, J. Mater. Chem. A 3 (2015) 12482–12499, https://doi.org/10.1039/C5TA01961C.

[75] A. Hanif, T. Xiao, A.P.E. York, J. Sloan, M.L.H. Green, Study on the structure and formation mechanism of molybdenum carbides, Chem. Mater. 14 (2002) 1009–1015, https://doi.org/10.1021/cm011096e.

[76] K. Oshikawa, M. Nagai, S. Omi, Characterization of molybdenum carbides for methane reforming by TPR, XRD, and XPS, J. Phys. Chem. B 105 (2001) 9124–9131, https://doi.org/10.1021/jp0111867.

[77] W. Xu, P.J. Ramírez, D. Stacchiola, J.L. Brito, J.A. Rodriguez, The carburization of transition metal molybdates (MₓMoO₄, M = Cu, Ni or Co) and the generation of highly active metal/carbide catalysts for CO₂ hydrogenation, Catal. Lett. 145 (2015) 1365–1373, https://doi.org/10.1007/s10562-015-1540-5.

[78] C.G. Silva, F.B. Passos, V.T. da Silva, Influence of the support on the activity of a supported nickel-promoted molybdenum carbide catalyst for dry reforming of methane, J. Catal. 375 (2019) 507–518, https://doi.org/10.1016/j.jcat.2019.05.024.

[79] K.T. Jung, W.B. Kim, C.H. Rhee, J.S. Lee, Effects of transition metal addition on the solid-state transformation of molybdenum trioxide to molybdenum carbides, Chem. Mater. 16 (2004) 307–314, https://doi.org/10.1021/cm030395w.

[80] A. Zhang, A. Zhu, B. Chen, S. Zhang, C. Au, C. Shi, In-situ synthesis of nickel modified molybdenum carbide catalyst for dry reforming of methane, Catal. Commun. 12 (2011) 803–807, https://doi.org/10.1016/j.catcom.2011.01.019.

[81] H. Zou, S. Chen, J. Huang, Z. Zhao, Effect of additives on the properties of nickel molybdenum carbides for the tri-reforming of methane, Int. J. Hydrog. Energy 41 (2016) 16842–16850, https://doi.org/10.1016/j.ijhydene.2016.07.108.

[82] L. Nie, P.M. de Souza, F.B. Noronha, W. An, T. Sooknoi, D.E. Resasco, Selective conversion of m-cresol to toluene over bimetallic Ni–Fe catalysts, J. Mol. Catal. A: Chem. 388– 389 (2014) 47–55, https://doi.org/10.1016/j.molcata.2013.09.029.

[83] P.M. de Souza, R.C. Rabelo-Neto, L.E.P. Borges, G. Jacobs, B.H. Davis, T. Sooknoi, D.E. Resasco, F.B. Noronha, Role of Keto intermediates in the hydrodeoxygenation of phenol over Pd on oxophilic supports, ACS Catal. 5 (2015) 1318–1329, https://doi.org/10.1021/cs501853t.

[84] A.M. Barrios, C.A. Teles, P.M. de Souza, R.C. Rabelo-Neto, G. Jacobs, B.H. Davis, L. E.P. Borges, F.B. Noronha, Hydrodeoxygenation of phenol over niobia supported Pd catalyst, Catal. Today 302 (2018) 115–124, https://doi.org/10.1016/j.cattod.2017.03.034.

[85] C.A. Teles, R.C. Rabelo-Neto, J.R. de Lima, L.V. Mattos, D.E. Resasco, F.B. Noronha, The effect of metal type on hydrodeoxygenation of phenol over silica supported catalysts, Catal. Lett. 146 (2016) 1848–1857, https://doi.org/10.1007/s10562-016-1815-5.

[86] P.M. de Souza, R.C. Rabelo-Neto, L.E.P. Borges, G. Jacobs, B.H. Davis, D. E. Resasco, F.B. Noronha, Hydrodeoxygenation of phenol over Pd catalysts. Effect of support on reaction mechanism and catalyst deactivation, ACS Catal. 7 (2017) 2058–2073, https://doi.org/10.1021/acscatal.6b02022.

[87] C.A. Teles, R.C. Rabelo-Neto, G. Jacobs, B.H. Davis, D.E. Resasco, F.B. Noronha, Hydrodeoxygenation of phenol over zirconia-supported catalysts: the effect of metal type on reaction mechanism and catalyst deactivation, ChemCatChem 9 (2017) 2850–2863, https://doi.org/10.1002/cctc.201700047.

[88] Q. Tan, G. Wang, A. Long, A. Dinse, C. Buda, J. Shabaker, D.E. Resasco, Mechanistic analysis of the role of metal oxophilicity in the hydrodeoxygenation of anisole, J. Catal. 347 (2017) 102–115, https://doi.org/10.1016/j.jcat.2017.01.008.

[89] C.A. Teles, P.M. de Souza, A.H. Braga, R.C. Rabelo-Neto, A. Teran, G. Jacobs, D. E. Resasco, F.B. Noronha, The role of defect sites and oxophilicity of the support on the phenol hydrodeoxygenation reaction, Appl. Catal. B: Environ. 249 (2019) 292–305, https://doi.org/10.1016/j.apcatb.2019.02.077.

[90] C.A. Teles, P.M. de Souza, R.C. Rabelo-Neto, A. Teran, G. Jacobs, D.E. Resasco, F. B. Noronha, Hydrodeoxygenation of lignin-derived compound mixtures on Pd-supported on various oxides, ACS Sustain. Chem. Eng. 9 (2021) 12870–12884, https://doi.org/10.1021/acssuschemeng.1c03720.

[91] P.M. de Souza, L. Nie, L.E.P. Borges, F.B. Noronha, D.E. Resasco, Role of oxophilic supports in the selective hydrodeoxygenation of m-Cresol on Pd catalysts, Catal. Lett. 144 (2014) 2005–2011, https://doi.org/10.1007/s10562-014-1337-y.